

**Electrotonic signal processing in AII amacrine cells: Compartmental models and passive membrane properties for a gap junction-coupled retinal neuron**

Bas-Jan Zandt, Margaret Lin Veruki and Espen Hartveit

University of Bergen, Department of Biomedicine, Bergen, Norway.

**Corresponding author:** Espen Hartveit, University of Bergen, Department of Biomedicine, Jonas Lies vei 91, N-5009 Bergen, Norway.

Email: [espen.hartveit@biomed.uib.no](mailto:espen.hartveit@biomed.uib.no)

Phone: +47-55586350

Fax: +47-55586360

**Running title:** Electrotonic signal processing in AII amacrine cells

**Number of figures:** 9

**Number of tables:** 2

**Key words:** retina; amacrine cell; compartmental model; electrotonic; passive membrane properties; dendrites.

Acknowledgement is given to the original source of publication. The final publication is available at:  
<https://link.springer.com/article/10.1007%2Fs00429-018-1696-z>

## Abstract

Amacrine cells are critical for processing of visual signals, but little is known about their electrotonic structure and passive membranes properties. AII amacrine cells are multifunctional interneurons in the mammalian retina and essential for both rod- and cone-mediated vision. Their dendrites are the site of both input and output chemical synapses and gap junctions that form electrically coupled networks. This electrical coupling is a challenge for developing realistic computer models of single neurons. Here, we combined multiphoton microscopy and electrophysiological recording from dye-filled AII amacrine cells in rat retinal slices to develop morphologically accurate compartmental models. Passive cable properties were estimated by directly fitting the current responses of the models evoked by voltage pulses to the physiologically recorded responses, obtained after blocking electrical coupling. The average best-fit parameters (obtained at -60 mV and ~25°C) were  $0.91 \mu\text{F}\cdot\text{cm}^{-2}$  for specific membrane capacitance,  $198 \Omega\cdot\text{cm}$  for cytoplasmic resistivity, and  $30 \text{k}\Omega\cdot\text{cm}^2$  for specific membrane resistance. We examined the passive signal transmission between the cell body and the dendrites by the electrotonic transform and quantified the frequency-dependent voltage attenuation in response to sinusoidal current stimuli. There was significant frequency-dependent attenuation, most pronounced for signals generated at the arboreal dendrites and propagating towards the soma and lobular dendrites. In addition, we explored the consequences of the electrotonic structure for interpreting currents in somatic, whole-cell voltage-clamp recordings. The results indicate that AII amacrines cannot be characterized as electrotonically compact and suggest that their morphology and passive properties can contribute significantly to signal integration and processing.

## Introduction

Signal integration is a fundamental function of neurons and involves the transformation of synaptic inputs to synaptic outputs (reviewed by Koch 1999; Spruston et al. 2016). The properties that shape this integration for a specific neuron are determined by its morphology and physiological characteristics, including both passive properties (membrane and cytoplasmic) and voltage- and ligand-gated ion channels. The majority of neurons in the mammalian central nervous system are variants of a prototypical morphology with a dendritic tree and an axon attached to the cell body (Cajal 1909, 1911). With this basic morphological plan, synaptic integration takes place in the dendritic tree and the cell body, with output mediated by action potentials generated in a discrete subcellular compartment (the axon initial segment; AIS), typically situated at the transition between the cell body and the axon (reviewed by Kole and Stuart 2012).

Amacrine cells, a class of interneurons in the retina, differ markedly from this prototypical morphology (Cajal, 1893). They generally do not possess an axon and their synaptic inputs and outputs are distributed over the dendritic tree such that synapses carrying information in opposite directions are found in close proximity, thereby enabling complex processing in local microcircuits (reviewed by Diamond 2017). For such cells, the cell body no longer plays a privileged role for integrating synaptic inputs and generating action potentials. Despite these common features, the ~45 - 50 different types of retinal amacrine cells display highly varied morphologies (Helmstaedter et al. 2013; for recent reviews, see Masland 2012; Diamond 2017). Thus, as for neurons in general, it is of great interest to understand how the morphology and electrotonic properties of specific amacrine cells contribute to their functional role in retinal signal processing. The narrow-field AII amacrine cell is by numbers the most common type of amacrine cell in the mammalian retina (~11%; Strettoi and Masland 1996) and plays a significant role for signal processing in both rod- and cone-mediated vision (Diamond 2017). An AII amacrine receives glutamatergic synaptic inputs from rod bipolar and OFF-cone bipolar cells and forms electrical synapses mediated by gap

junctions with ON-cone bipolar cells and other AII amacrine cells (reviewed by Hartveit and Veruki 2012). AII amacrine cells are themselves inhibitory and provide chemical (glycinergic) synapses onto OFF-cone bipolar cells and OFF-ganglion cells (Kolb and Famiglietti 1974; Strettoi et al. 1992). In this way, AII amacrine cells are positioned to distribute rod pathway visual signals into both ON- and OFF-channels of the cone pathways and to provide cross-over inhibition between ON- and OFF-pathways (Manookin et al. 2008; Münch et al. 2009; Murphy and Rieke 2008).

Whereas the AII cells have relatively small dendritic trees, detailed quantitative analysis recently revealed that the extent of branching is considerably larger than suggested by earlier investigations (Zandt et al. 2017). The dendritic tree is bi-stratified with arboreal and lobular dendrites in the proximal and distal part of the inner plexiform layer, respectively. Importantly, specific types of input and output synapses are segregated across the different parts of the dendritic tree; the connections with rod bipolar cells, ON-cone bipolar cells and other AII amacrine cells are located in the arboreal dendrites and the connections with OFF-cone bipolar cells and OFF-ganglion cells are located in the lobular dendrites. The complex connectivity and segregation of both chemical and electrical synaptic connections raise the question of how AII amacrine cells integrate and process visual signals. It has been suggested that the AII amacrine is an electrotonically compact neuron (Vardi and Smith 1996; Schubert and Euler 2010; Cembrowski et al. 2012; Diamond 2017), but the issue remains controversial and combined experimental and computational analysis of the spiking behavior of AII amacrine cells has suggested that at least one distinct process is electrotonically remote from the rest of the cell (Cembrowski et al. 2012; Choi et al. 2014). To our knowledge there are no published investigations of the electrotonic properties of these cells, including estimates of their passive membrane properties, based on compartmental models developed with morphologically realistic and detailed reconstructions of electrophysiologically characterized cells.

Here, as a first step towards investigating signal transfer and integration in AII amacrine cells, we developed multicompartment models of these cells by

simultaneously acquiring electrophysiological responses and multi-photon excitation (MPE) microscopic images of AII amacrine cells filled with a fluorescent dye during whole-cell recording in rat retinal slices. In addition to standard pharmacological blockers of voltage- and ligand-gated ion channels to make the cells behave passively, we blocked gap junctions pharmacologically to obtain adequately correlated morphological and physiological data. Following quantitative morphological reconstruction, we estimated the passive membrane properties of AII amacrine cells by directly fitting the responses of the compartmental models evoked by voltage pulses to the current responses evoked in the physiological recordings. We then used the compartmental models to study electrotonic transmission of passive signals generated and recorded at various locations in the cells and to study the extent of space-clamp control in voltage-clamp recordings. Our results suggest that the AII amacrine cannot be characterized as electrotonically compact. These compartmental models represent a significant advance compared to previous simplified models and will facilitate computational studies of signal integration and processing in AII amacrine cells, including the future development of detailed compartmental models that incorporate voltage- and ligand-gated ion channels as well as electrical coupling via gap junctions.

## **Materials and methods**

### **Retinal slice preparation**

Various aspects of the methods have previously been described in detail (Oltedal et al. 2009; Zandt et al. 2017). The use of animals in this study was carried out under the approval of and in accordance with the regulations of the Animal Laboratory Facility at the Faculty of Medicine at the University of Bergen (accredited by AAALAC International). Wistar HanTac rats (female, albino; 5 - 7 weeks postnatal) were purchased from Taconic Bioscience (Denmark), had *ad libitum* access to food and water and were kept on a 12/12 light/dark cycle. Animals ( $n = 11$ ) were deeply anaesthetized with isoflurane (IsoFlo vet 100%; Abbott Laboratories Ltd, Maidenhead, UK) in 100% O<sub>2</sub> and killed by cervical dislocation. Both eyes were removed and the retina was

dissected out of each eye under a dissection microscope. Retinal slices were cut by hand with a curved scalpel blade at a thickness of ~100 to ~150  $\mu\text{m}$ . For MPE microscopic imaging, slices were visualized using a custom-modified "Movable Objective Microscope" (MOM; Sutter Instrument, Novato, CA, USA) with a  $\times 20$  water immersion objective (XLUMPLFL; 0.95 NA; Olympus) and infrared Dodt gradient contrast videomicroscopy (IR-DGC; Luigs & Neumann, Ratingen, Germany), using an IR-sensitive analog CCD camera (VX55; TILL Photonics, Gräfelfing, Germany). The cell bodies of the recorded cells were generally located 20 - 30  $\mu\text{m}$  below the surface of the slice. Electrophysiological recording and imaging were carried out at room temperature and for each experiment the temperature was monitored continuously at the recording chamber. The average temperature was  $24.6 \pm 0.2^\circ\text{C}$  (S.D.) and ranged between 24.3 and 25.0 $^\circ\text{C}$ . The fluctuation within a single experiment was approximately 0.1 $^\circ\text{C}$ .

### **Solutions and drugs**

The extracellular perfusing solution was continuously bubbled with 95%  $\text{O}_2$  - 5%  $\text{CO}_2$  and had the following composition (in mM): 125 NaCl, 25  $\text{NaHCO}_3$ , 2.5 KCl, 2.5  $\text{CaCl}_2$ , 1  $\text{MgCl}_2$ , 10 glucose, pH 7.4. The recording pipettes were filled with an intracellular solution of the following composition (in mM): 125 K-gluconate, 5 KCl, 8 NaCl, 0.2 EGTA, 10 HEPES, 4 MgATP, and 0.4 NaGTP (pH adjusted to 7.3 with KOH). The pipette solution also contained Alexa Fluor 594 hydrazide as sodium salt (40 or 60  $\mu\text{M}$ ; Invitrogen). The osmolality was  $\sim 290 \text{ mOsmol} \cdot \text{kg}^{-1} \text{ H}_2\text{O}$ . The data acquisition software (Patchmaster; HEKA Elektronik, Lambrecht / Pfalz, Germany) corrected all holding potentials for the liquid junction potential on-line. Theoretical liquid junction potentials were calculated with JPCalcW (Axon Instruments, Union City, CA, USA).

Drugs were added directly to the extracellular solution used to perfuse the slices. The concentrations of drugs were as follows ( $\mu\text{M}$ ; supplier Tocris Bioscience, Bristol, UK, unless otherwise noted): 10 bicuculline methchloride, 10 6-cyano-7-nitroquinoxaline-2,3-dione (CNQX), 1 strychnine (Research Biochemicals Inc., Natick,

MA, USA), 20 3-((*RS*)-2-carboxypiperazin-4-yl)-propyl-1-phosphonic acid (CPP), 1 tetrodotoxin (TTX), 30 4-ethylphenylamino-1,2-dimethyl-6-methylaminopyrimidinium chloride (ZD7288), 100 2-[(2,6-dichloro-3-methylphenyl)amino]benzoic acid sodium salt (meclofenamic acid [MFA] sodium salt; Sigma-Aldrich).

### **Electrophysiological recording and data acquisition**

Patch pipettes were pulled from thick-walled borosilicate glass (outer diameter, 1.5 mm; inner diameter, 0.86 mm). Electrodes were coated with Parafilm (American National Can; Greenwich, CT, USA) almost to the tip to reduce their capacitance. In addition, the fluid level both in the recording chamber and in the pipette was kept as low as possible to minimize the electrode capacitance. The open-tip resistance of the pipettes ( $R_{\text{pip}}$ ) ranged between 7 and 9 M $\Omega$  when filled with intracellular solution. Whole-cell voltage-clamp recordings from AII amacrine cells were performed with an EPC10-triple amplifier (HEKA Elektronik) controlled by Patchmaster software. To keep the background fluorescence in the area immediately surrounding the cell body to a minimum, we only applied a small positive pressure to the pipette (5 - 10 mbar) to reduce the leakage of dye as we approached the cell. After establishing a G $\Omega$ -seal (2 - 25 G $\Omega$ ), currents caused by the recording electrode capacitance were automatically measured and neutralized by the amplifier ( $C_{\text{fast}}$  function of Patchmaster software). The average  $C_{\text{fast}}$  time constant was  $4.60 \pm 0.68$  pF (range 3.62 - 5.75 pF;  $n = 13$  cells). After breaking into a cell, currents caused by the cell membrane capacitance were partially neutralized by the amplifier ( $C_{\text{slow}}$  function of Patchmaster software).

Whole-cell voltage-clamp recording was used to sample measurements of capacitive current transients, to monitor pharmacological block of voltage-gated Na<sup>+</sup> channels and spontaneous synaptic inputs, and to monitor the series resistance ( $R_s$ ), as automatically determined by the Patchmaster software, online throughout the recording. For sampling capacitive current transients, the  $C_{\text{slow}}$  capacitance neutralization circuitry was transiently disabled and the time constant of the internal stimulus filter was set to 2  $\mu$ s.  $R_s$  was not compensated and was included as a free

parameter in the off-line modeling (see below). The sampling interval was set to  $10\ \mu\text{s}$  and before sampling, signals were low-pass filtered (analog 3-pole Bessel filter) with a corner frequency (-3 dB) of 30 kHz (10 kHz for one cell) to minimize the effect of any introduced timing errors on model fitting (see below). Current transients were evoked by 20 ms long voltage pulses of alternating amplitudes of  $\pm 5$  or  $\pm 10$  mV from the holding potential of -60 mV (slightly more negative than the resting membrane potential). When we sampled other current responses, the  $C_{\text{slow}}$  capacitance neutralization circuitry was re-enabled and the time constant of the internal stimulus filter was set to  $20\ \mu\text{s}$ . Signals were low-pass filtered (analog 3- and 4-pole Bessel filters in series) with a corner frequency (-3 dB) set to  $1/5$  of the inverse of the sampling interval (50 -  $100\ \mu\text{s}$ , depending on protocol).

Whole-cell current-clamp recording was used to sample measurements of voltage responses to short (2 ms) and long (500 ms) depolarizing and hyperpolarizing current pulses. Because of the high input resistance of AII amacrine cells after blocking gap junction coupling pharmacologically (see below; Veruki et al. 2010), the membrane potential displayed considerable fluctuation. To compensate for this and to stabilize the membrane potential, we used the low-frequency voltage-clamp (LFVC) function in Patchmaster (Peters et al. 2000). This is a modified current-clamp mode that allows current-clamp measurement of fast voltage transients while the average potential is kept constant with a slow voltage clamp (set to -60 mV for the AII amacrine recordings). To avoid distortion of the response to short and long current pulses, we used the slowest time constant ( $\sim 100\ \text{s}$ ) of the LFVC function.

To verify the ability of MFA to block electrical coupling of AII amacrine cells in whole-cell recordings with standard (low-resistance) pipettes, we targeted pairs of neighboring cells in retinal slices (Veruki and Hartveit 2002a) visualized using an Olympus BX51WI microscope with a  $\times 60$  water immersion objective and IR differential interference contrast videomicroscopy. Recording and data acquisition were performed as described earlier for single cells, but when we recorded currents caused by the pipette and cell membrane capacitance, the test pulse stimuli were sent

simultaneously to both recording amplifiers to eliminate junctional currents between the two cells. Throughout these recordings, the  $R_s$  in both cells was regularly monitored by applying a series of hyperpolarizing voltage pulses (-20 mV, 16 ms duration). During such stimulation, the  $C_{\text{slow}}$  neutralization circuitry was transiently disabled and the stimulus was simultaneously sent to both amplifiers. Capacitative transients were analyzed on- and off-line by averaging consecutive responses ( $n = 100$ ) and fitting the decay with double-exponential functions to estimate the peak capacitative current and calculate the  $R_s$ . For the calculation of the junctional conductance ( $G_j$ ) between the two cells, we corrected for non-zero  $R_s$  and finite membrane resistance ( $r_m$ ; for details, see Hartveit and Veruki 2010).

### **Image acquisition for MPE microscopy and wide-field fluorescence microscopy**

For MPE microscopy, fluorescence from neurons filled with Alexa 594 was imaged with the MOM equipped with a mode-locked Ti:sapphire laser (Mai Tai DeepSee; SpectraPhysics, Irvine, CA, USA) tuned to 810 nm. Scanning was performed by galvanometric scanners (XY; Cambridge Technology, Cambridge, MA, USA), fluorescence was detected by multialkali photomultiplier tubes (R6357; Hamamatsu Corp., Bridgewater, NJ, USA), and the analog signals were digitized by an acquisition board (NI-6110E; National Instruments, Austin, TX, USA). The intensity of the laser was attenuated and controlled by an electro-optic modulator (350-80LA with BK option; ConOptics, Danbury, CT, USA) driven by a 302RM amplifier (ConOptics). During image acquisition, exposure to IR laser light was controlled by an electronic shutter (LS6ZM2; Vincent Associates, Rochester, NY, USA), thereby minimizing the total exposure time. An image stack was acquired as a series of optical sections ( $1024 \times 1024$  pixels) with XY pixel size  $\sim 70$  to  $\sim 80$  nm (depending on the magnitude of the digital zoom factor) and collected at a focal plane interval of  $0.4 \mu\text{m}$ , sufficient to satisfy Nyquist rate sampling (for details, see Zandt et al. 2017). For each image stack, we acquired two channels and at each focal plane two images were averaged on-line. The first channel sampled the fluorescence light as described above. The second channel

was used for IR laser scanning gradient contrast imaging (IR-LSGC; Yasuda et al. 2004) and sampled the forward scattered IR laser light after it passed the substage condensor and a Dodt gradient contrast tube (Luigs & Neumann). MPE microscopy and image acquisition were controlled by ScanImage software (version 3.8.1; Polgruto et al. 2003) running under Matlab (The Mathworks, Natick, MA, USA).

In the experiments with simultaneous dual recording of pairs of electrically coupled AII amacrine cells, we used wide-field fluorescence microscopy to acquire image stacks of the cells filled with Alexa 594 via the patch pipettes (TILLvISION system with a Polychrome V light source and an Imago QE cooled CCD camera; TILL Photonics; for a detailed description, see Castilho et al. 2015).

### **Image processing and spatial deconvolution**

Image stacks were de-interleaved based on acquisition channels (IGOR Pro, 64-bit; WaveMetrics, Lake Oswego, OR, USA) and saved as individual files (one per channel). The complete fluorescence image stack was processed in Huygens Essential (64 bit; Scientific Volume Imaging, Hilversum, The Netherlands) to remove noise and reassign out-of-focus light with a theoretically calculated point spread function, using the Classic Maximum Likelihood Estimation (CMLE) algorithm for spatial deconvolution. For image stacks acquired with MPE microscopy, the Object Stabilizer module of Huygens Essential was used to align image slices along the Z-axis to compensate for drift and other mechanical instabilities. Processed image stacks were saved in 16-bit TIFF format, utilizing the whole dynamic range. For additional details, see Zandt et al. (2017).

### **Three-dimensional (3D) reconstructions and quantitative morphological measurements**

Quantitative morphological reconstruction of the fluorescently labeled cells was done with NeuroLucida software (64 bit; MBF Bioscience, Williston, VT, USA) running under Windows 7 Pro 64-bit (for a detailed description, see Zandt et al. 2017). The 3D

reconstruction of the soma was made by tracing it with multiple contours at a series of different focal planes. The NeuroLucida data files containing the quantitative morphological representation of each reconstructed neuron were imported to NEURON using the *Import3D* tool. For the soma, the major axis of the soma single contour was used to slice it into a series of disks from edge to edge (along the minor axis). The disks would then slide on the plane normal to the major axis to remove all the curvature of the centroid and the resulting cylindrically symmetric shape was then used for the quantitative simulations. In addition, functions in NEURON were used to calculate the surface area of the soma and of the complete morphology of the cell.

### **Computer modeling and simulation**

Computer simulations of passive cable models were performed with NEURON (version 7.3; Carnevale and Hines 2006) running under Mac OS X (10.9.5). To save computation time, a time step of 25  $\mu\text{s}$  was first used to obtain a rough estimate of the best-fitting model parameters, after which the fit was refined using a time step of 2.5  $\mu\text{s}$ . Such a small time step was necessary to correctly calculate the charge injected during the first  $\sim 100 \mu\text{s}$  after the onset of the voltage step. For analysis, data generated during the fitting procedure were downsampled to give a sampling interval of 10  $\mu\text{s}$ , equal to that of the recorded data traces. Spatial discretization (compartmentalization) was implemented by applying the *d\_lambda* rule (Carnevale and Hines 2006). Briefly, the alternating current (AC) length constant at 100 Hz ( $\lambda_{100}$ ) was calculated for each section (branch, i.e. a continuous length of unbranched cable) and the number of segments (*nseg*) in each section was adjusted such that the length of each segment was smaller than a fraction *d\_lambda* of  $\lambda_{100}$ . For all simulations, the fraction was set to 0.1 by the adjustable parameter *d\_lambda*. These segment lengths were calculated using NEURON's standard values for specific membrane capacitance ( $C_m$ ;  $1.0 \mu\text{F} \cdot \text{cm}^{-2}$ ), specific membrane resistance ( $R_m$ ;  $1000 \Omega \cdot \text{cm}^2$ ), and cytoplasmic (internal) resistivity ( $R_i$ ;  $35.4 \Omega \cdot \text{cm}$ ). This resulted in almost all branch sections being modeled with a

single compartment. Corresponding to this, the average number of sections was  $390 \pm 120$  (S.D.; range = 210 - 624) and the average number of segments was  $400 \pm 110$  (S.D.; range = 213 - 635;  $n = 13$  cells with full morphological reconstruction). These values are very similar to those obtained for the larger (albeit partially overlapping) population of AII amacrine cells in a previous study from our laboratory where the average number of sections was 343 (range = 110 - 630;  $n = 43$  cells; Zandt et al. 2017). Using smaller compartments did not change the simulation results appreciably. In the simulations, an idealized single-electrode voltage clamp (SEClamp; taken from the standard repertoire of NEURON point processes) was connected to the soma compartment (at which the recording pipette was located during electrophysiological recording). Before each simulation run, the model was initialized to steady-state (Carnevale and Hines 2006). For quantitative analysis of signal transmission between different cellular compartments, all 13 cells were used.

Passive membrane parameters were obtained using NEURON's Multiple Run Fitter (MRF) to directly fit (Clements and Redman 1989) the current responses of a given morphological model evoked by voltage pulses to the physiological data obtained for the same cell. The MRF tool uses the principal axis (PRAXIS) algorithm (Brent 1973) to minimize the sum of squared errors ( $\chi^2$ ) between the model current response to voltage pulses and the experimental data. Four free parameters were included in the fitting:  $C_m$ ,  $R_m$ ,  $R_i$  (each assumed to be uniform throughout the neuron), and  $R_s$  (specified for the SEClamp point process in NEURON). Because the initial seal resistance was  $> 2 \text{ G}\Omega$ , it is likely that the seal remained intact during recording. In similar recordings, slow withdrawal of the recording pipette results in the formation of an outside-out patch (e.g. Veruki et al. 2003). Accordingly, a shunt at the recording electrode was not included in the model. For fitting, we typically used the following starting values:  $R_s = 10 \text{ M}\Omega$ ,  $R_i = 100 \text{ }\Omega \cdot \text{cm}$ ,  $C_m = 1.0 \text{ }\mu\text{F} \cdot \text{cm}^2$  and  $R_m = 10 \text{ k}\Omega \cdot \text{cm}^2$  (corresponding to a specific membrane conductance,  $G_m$ , of  $1.0 \times 10^{-4} \text{ S} \cdot \text{cm}^{-2}$ ). The reversal potential ( $E_{\text{rev}}$ ) of the leak current (e\_pas) was set to the holding potential used during acquisition of the experimental traces. Only current responses evoked by the

negative voltage pulses (-5 and -10 mV from  $V_{\text{hold}}$ ) were used for the direct fitting (see below). Fitting was started from 0.4 ms after onset of the voltage pulse to avoid artifacts from filtering and  $C_{\text{fast}}$  compensation. The rest of the 20 ms period following the onset of the voltage step was weighted equally for the fitting. We verified that weighting the initial part of the current traces more heavily (by a factor of 10), did not change the results appreciably. Experimental traces were zero-subtracted before the direct fitting procedure. As an additional check that purely passive responses were measured, several series of voltage steps were evoked at holding potentials of -65, -70, and/or -75 mV (for five cells). We verified that the difference in holding potential did not cause the fitted parameters or  $V_{\text{rest}}$  (see below) to change. Finally, we checked whether delays of the recorded traces, potentially introduced by low-pass filtering or the neutralization of the recording electrode capacitance had an effect on the fitted parameters. Shifting the recorded traces by 10  $\mu\text{s}$  in either direction (relative to the voltage pulse) resulted in relatively small changes in the fitted parameters for  $C_{\text{m}}$  (~2%),  $R_{\text{m}}$  (~0.3%),  $R_{\text{i}}$  (~2%) and  $R_{\text{s}}$  (~10%). Because the effects were relatively small compared to either the corresponding random error or the error introduced by uncertainty in the dendritic diameters, we did not take these further into account. For two cells, unrealistically low values for  $R_{\text{s}}$  were obtained from the fitting ( $R_{\text{s}} \leq R_{\text{pip}} \times 2$ ). For these two cells, a lower bound on  $R_{\text{s}}$  was set at  $R_{\text{pip}} \times 2$  during fitting.

To verify that the fitting routine was able to retrieve the best-fitting parameters without getting stuck in local minima, we tested it with synthetic data generated from one of the AII amacrine cell compartmental models. For this testing, initial parameter values were varied over a wide range (by a factor of ~10). In the large majority of runs, the algorithm recovered the original parameters. Only rarely did the fitting converge to a solution that corresponded to a local minimum. However, in these cases the obtained parameters were always clearly outside the relevant biological range ( $C_{\text{m}} > 2.0 \mu\text{F} \cdot \text{cm}^{-2}$  and  $R_{\text{i}} > 1000 \Omega \cdot \text{cm}^2$ ) and resulted in a bad fit to the data. When this occurred during fitting to physiological responses (5 fits out of ~1500), initial conditions were simply

changed (which was more practical than implementing e.g. a simulated annealing algorithm).

Synaptic conductance waveforms injected into the theoretical computer models were modeled as an error function multiplied with an exponential decay:

$$g_{syn}(t) = g_0 \times a \left( (1 + \operatorname{erf}((t - \delta)/\tau_{rise} - 2)) \times \exp(-(t - \delta)/\tau_{decay}) \right) \quad \text{for } t \geq 0$$

$$g_{syn}(t) = 0 \quad \text{for } t < 0$$

where  $g_0$  is the peak conductance,  $\delta$  is the delay to onset,  $\tau_{rise}$  is the rise time constant,  $\operatorname{erf}$  is the error function,  $\tau_{decay}$  is the decay time constant, and  $a$  is a scaling factor to scale the peak of the expression within the parenthesis to 1. We found that this waveform could closely reproduce the shape of experimentally recorded spontaneous excitatory postsynaptic currents (spEPSCs) in AII amacrine cells (Veruki et al., 2003). At room temperature, spEPSCs in these cells have an average 10 - 90% rise time of  $\sim 340 \mu\text{s}$ , decay time constant of  $\sim 760 \mu\text{s}$  (when fitted with a single exponential), and peak amplitude of  $\sim 29 \text{ pA}$  (at  $V_{\text{hold}} = -60 \text{ mV}$ ; Veruki et al., 2003). An average spEPSC obtained from a single cell with properties close to the population average was selected and the parameters of the equation were fitted to closely reproduce this spEPSC. In this way, we obtained  $g_0 = 480 \text{ pS}$  (corresponding to a  $29 \text{ pA}$  current for a  $60 \text{ mV}$  driving force),  $\tau_{rise} = 224 \mu\text{s}$  (corresponding to a 10 - 90% rise time of  $340 \mu\text{s}$ ), and  $\tau_{decay} = 760 \mu\text{s}$ .

### **Error analysis**

The accuracy of the obtained parameters was assessed by estimating both the random error and the systematic error (see Results). The random error was determined by bootstrapping. For each cell, balanced resampling was done by generating 1000 bootstrap traces by randomly selecting traces (with repetition) from the individual averages used to generate the original grand average. Each bootstrap trace was the average of  $N$  traces with  $N$  equal to the number of traces in the original data set for a given cell. The 1000 synthetic data sets were used for model fitting in NEURON to

obtain 1000 best-fit values for  $C_m$ ,  $R_m$ , and  $R_i$  and the coefficient of variation (CV; mean/S.D.) for each parameter.

### **Statistical analysis and data presentation**

In addition to NEURON, data were analyzed with NeuroLucida Explorer (MBF Bioscience), Fitmaster (HEKA Elektronik) and IGOR Pro. For correlation analysis, we calculated Pearson's correlation coefficient  $R$  and report the coefficient of determination, i.e., the squared value  $R^2$ . Data are presented as means  $\pm$  S.D. ( $n$  = number of cells). The number of individual traces included in the averaged current or voltage traces in the figures are stated for each case.

## **Results**

### **Targeting, electrophysiological recording, and imaging of AII amacrine cells**

AII amacrine cells in retinal slices were identified and targeted for recording with IR-DGC videomicroscopy incorporated into the optical pathways of the MPE microscope (Fig. 1a). The visual criteria included the location of the cell body deep in the inner nuclear layer (at the border between this layer and the inner plexiform layer) and the presence of a thick apical dendrite descending into the inner plexiform layer. The electrophysiological criterion was the presence of characteristic depolarization-evoked, inward action currents (Fig. 1b), immediately observed following the establishment of the whole-cell recording configuration during application of 5 mV depolarizing test pulses (from  $V_{\text{hold}} = -60$  mV). These action currents correspond to unclamped action potentials that depend on voltage-gated  $\text{Na}^+$  channels (Mørkve et al. 2002). After a few minutes, sufficient dye had diffused into the cells to allow visual verification as an AII amacrine cell with MPE microscopy and fluorescence imaging (Fig. 1c).

*Fig. 1 near here*

## **MPE microscopic imaging and morphological reconstruction**

To ensure that the morphology obtained by structural imaging corresponded to that of single cells, we used non-gap junction permeable fluorescent dyes instead of tracers such as biocytin and Neurobiotin that permeate the gap junctions between AII amacrine cells and between AII amacrine and ON-cone bipolar cells (Vaney 1991; Hampson et al. 1992; Mills and Massey 1995; Trexler et al. 2001). Structural imaging was done by MPE fluorescence microscopy to obtain high-resolution morphology (cf. Zandt et al. 2017) and was performed in parallel with the electrophysiological recording. Approximately 10 - 15 min after breaking into the cell, we started acquiring an image stack. A complete stack, sampled at a resolution that satisfied the Nyquist sampling criteria in both XY and Z, required a total of 120 - 200 slices with a focal plane interval of 0.4  $\mu\text{m}$ . With an in-plane resolution of 1024  $\times$  1024 pixels for each slice and on-line averaging of two frames per slice, acquisition of a complete stack required 25 - 30 min. Cells with suboptimal morphology (beading and/or truncated processes at the surface of the slice) were eliminated. The image stacks sampled with MPE fluorescence microscopy were deconvolved to remove noise and re-assign out-of-focus light (for details, see Zandt et al. 2017). The morphology of each cell was then reconstructed manually with the NeuroLucida system (Fig. 1d) and the digitized morphological data were imported to NEURON. Here we have obtained correlated electrophysiological and morphological data for a total of 13 AII amacrine cells (Fig. 1d). Eight of the 13 cells included in the present study were also included in an earlier report with a detailed morphometric analysis of AII amacrine cells (Zandt et al. 2017). The morphological properties of the additional five cells were similar to the others (Fig. 1d) and to the rest of the total population of cells studied by Zandt et al. (2017).

*Fig. 2 near here*

## **Using MFA to block electrical coupling of AII amacrine cells**

When determining the passive electrical properties of neurons, it is standard to use pharmacological agents to block ligand- and voltage-gated currents and make the cells

behave passively (Major 2001). In our recordings, we included drugs in the extracellular solution to block ligand-gated ion channels (CNQX to block non-NMDA receptors, CPP to block NMDA receptors, bicuculline to block GABA<sub>A</sub> receptors and strychnine to block glycine receptors) and voltage-gated ion channels (TTX to block  $I_{Na}$  and ZD7288 to block  $I_h$ ). However, for AII amacrine cells there is strong evidence from both morphological (Kolb and Famiglietti 1974; Strettoi et al. 1992, 1994) and functional (Veruki and Hartveit 2002a, 2002b) studies for electrical coupling via gap junctions, both between neighboring AII amacrine cells and between AII amacrine cells and ON-cone bipolar cells. Such coupling can be directly measured by dual, simultaneous recording of neighboring cells in retinal slices (Veruki and Hartveit 2002a, 2002b). In principle, with paired electrophysiological recording of electrically coupled cells, it is possible to estimate the magnitude of the conductance of the electrical coupling by applying the "2-cell circuit" model (Hartveit and Veruki 2010) and correcting the results for this value. However, there are two problems with this approach. First, it is strictly speaking only valid for single-compartment models. Second, when the 2-cell circuit is part of a larger network of electrically coupled cells, as for AII amacrine cells in the retina, the total membrane resistance (corresponding to the parameter  $r_m$  of the 2-cell circuit model) includes not only non-gap junctional resistance for each cell, but also gap junctional resistance between each of the two recorded cells and the other cells to which they are coupled, and is only an apparent membrane resistance. Therefore, our approach here was to directly block the electrical coupling by using the pharmacological agent MFA (100  $\mu$ M), previously demonstrated to block electrical coupling involving AII amacrine cells in recordings with high-resistance pipettes to reduce intracellular washout (Veruki and Hartveit 2009; Veruki et al. 2010). We verified this result here by recording from three pairs of electrically coupled AII amacrines with conventional (low-resistance) patch pipettes (Fig. 2a) and observed complete block of electrical coupling within 30 min (Fig. 2b). Consistent with previous results from our laboratory (Veruki et al. 2010), MFA also evoked an increase of the apparent membrane resistance ( $r_m$ ; as estimated with the "2-cell circuit" model; Fig. 2c)

and in most cases a reduction of the negative holding current (at a holding potential of -60 mV; Fig. 2d). There was no consistent change of the  $R_s$  related to the application of MFA. In this condition, the passive responses of AII amacrine cells should be functionally isolated and reflect only non-gap junctional resistance.

*Fig. 3 near here*

### **Linearity of current responses to small voltage steps**

To develop a passive cable model of a cell studied in voltage-clamp, it is necessary to ensure that the current response of the cell scales linearly with the applied voltage, without activation or deactivation of voltage-gated currents. In addition to voltage-gated  $\text{Na}^+$  channels (blocked here by TTX), there is evidence that AII amacrine cells express voltage-gated  $\text{K}^+$  channels (Boos et al. 1993). Tian et al. (2010) found evidence for high voltage-activated A-type  $\text{K}^+$  channels, with a half-activation voltage of around +10 mV, but with a wide activation curve. Although the largest activation was observed at membrane potentials more depolarized than -40 mV, some degree of activation was observed already at -50 mV. Cembrowski et al. (2012) found evidence for M-type currents, with activation at membrane potentials more depolarized than -55 mV. AII amacrine cells also express voltage-gated  $\text{Ca}^{2+}$  channels of the L-type, with molecular specificity corresponding to  $\alpha$ -1D /  $\text{Ca}_v1.3$  and an activation threshold between -60 and -50 mV (Habermann et al. 2003). These channels are predominantly, but perhaps not exclusively, localized to the appendages of the lobular dendrites (Habermann et al. 2003; Balakrishnan et al. 2015). Accordingly, we considered that with a combination of pharmacological blockers and a membrane holding potential ( $V_{\text{hold}}$ ) of -60 mV, it should be possible to apply low-amplitude voltage pulses without significant activation of voltage-gated currents.

During a recording, we switched to an extracellular solution with drugs to block ligand- and voltage-gated ion channels 1 - 3 min after establishing the whole-cell recording configuration. As soon as we observed that the depolarization-evoked action currents (Fig. 1b) and spontaneous postsynaptic currents were completely blocked (~3

min after switching solutions), we started acquiring electrophysiological data by repeated sampling of the responses evoked by voltage pulses. After acquiring responses under baseline conditions (5 - 10 min), we switched to an extracellular solution that also contained MFA to block gap junction channels and continued electrophysiological sampling for a total of 40 - 60 min to ensure an adequate recording period during which gap junction channels were blocked (cf. Fig. 2).

We examined the linearity of the membrane current response to application of short (20 ms) hyperpolarizing and depolarizing steps of  $\pm 5$  and  $\pm 10$  mV from  $V_{\text{hold}} = -60$  mV (Fig. 3a). These voltage steps evoked transient current responses with steady-state components ranging from approximately  $\pm 7$  to approximately  $\pm 15$  pA (calculated as the average during the last 5 ms of the voltage pulse; Fig. 3a). For each voltage step ( $\pm 5$  and  $\pm 10$  mV) we calculated the average from 50 or 100 (depending on noise level) consecutive, baseline-subtracted responses. Only responses obtained after complete block of gap junction coupling by MFA were included in these averages. To evaluate the linearity of the membrane response, we scaled the average responses by dividing them by the amplitude of the corresponding voltage step and then superimposed them (Fig. 3b). The -5 and -10 mV hyperpolarizing voltage steps evoked responses that superimposed well with each other after appropriate scaling (Fig. 3b) and are therefore presumed to be linear and passive. For +5 and +10 mV depolarizing voltage steps, however, the evoked currents did not superimpose with each other or with the currents evoked by the hyperpolarizing voltage steps (Fig. 3b), suggesting weak activation of relatively slow, voltage-gated currents, potentially a combination of voltage-gated  $\text{Ca}^{2+}$  and  $\text{K}^{+}$  currents.

To quantify the linearity of evoked membrane currents, we plotted the average responses evoked by a given voltage step against the response evoked by the -5 mV voltage step (after appropriate scaling) for corresponding points in time after low-pass filtering at 1 kHz. For the cell illustrated in Fig. 3c, the slope was 0.98 when the data points were fitted with a straight line (-5 and -10 mV voltage steps). For all 13 cells, the corresponding slope (relative to the -5 mV steps) was  $1.002 \pm 0.013$  for the -10 mV

steps,  $0.976 \pm 0.010$  for the +5 mV steps, and  $0.963 \pm 0.025$  for the +10 mV steps. Taken together, we conclude that at  $V_{\text{hold}} = -60$  mV, only the responses to hyperpolarizing voltage pulses (to -65 or -70 mV) are passive without measurable activation or deactivation of voltage-gated membrane currents. Accordingly, we used only hyperpolarizing voltage pulses for subsequent analysis and model fitting.

*Fig. 4 near here*

### **Detailed cable models and passive membrane properties of AII amacrine cells**

To investigate the passive membrane properties of AII amacrine cells, we used NEURON to fit the current responses of the morphological model evoked by voltage pulses (to -65 and -70 mV from  $V_{\text{hold}} = -60$  mV) to the experimentally obtained current responses such that the responses generated by the model matched the experimental responses. Each electrophysiological response used during model optimization was obtained by averaging 50 or 100 individual responses (depending on the noise level) evoked by the voltage pulses (-5 and -10 mV). Model fitting was performed for each average of the responses to the negative voltage pulses. Fig. 4a shows examples of averaged current responses obtained before and after application of MFA to block electrical coupling via gap junctions. For each parameter ( $R_m$ ,  $C_m$ ,  $R_i$ , and  $R_s$ ) this generated a time series for the duration of the experiment. To preserve the peak current evoked by the voltage step, the electrophysiological responses were not additionally filtered during the offline analysis. The goodness-of-fit was estimated by the root-mean-square (RMS) of the fit residual, i.e., the difference between the physiologically recorded response and the response generated by the model (Fig. 4b, c). Because the RMS value of the fit residual was dominated by noise in the data, the fit error was defined as the RMS of the fit residual after low-pass filtering the residual at 1 kHz. At the beginning of the recording, when the AII amacrine cells were coupled to other cells by gap junctions, the fit residual deviated systematically from the zero line (with a relatively large RMS value; Fig. 4c, left panel), indicating that the model parameters did not provide a good fit to the experimental responses. However, over

the course of a recording, with gradually increasing block of the electrical coupling by MFA, the fit residual was eventually reduced to noise randomly distributed around the zero line and the error (RMS of fit residual) decreased (Fig. 4c, right panel). As illustrated by the example in Fig. 4d, the decrease of the error started within 5 min after switching to the extracellular solution containing MFA and most likely reflects the slowly developing block of gap junction coupling by MFA (Fig. 2). The pattern of alternating higher and lower errors (Fig. 4d) is the result of obtaining alternating responses evoked by -5 and -10 mV voltage steps, with the steps to -10 mV yielding responses with effectively lower noise because they were normalized to the responses to -5 mV (by dividing them by two).

The effect of blocking the gap junctions with MFA was also apparent as an increase in the estimate for  $R_m$  (Fig. 4e) and a decrease in the estimate for  $C_m$  (Fig. 4f). The initial estimates for  $R_m$  (before adding MFA) were relatively low, but slowly increased approximately four-fold towards a plateau after adding MFA (Fig. 4e). The increase of  $R_m$  occurred in parallel with an increase in input resistance (not shown; see Veruki et al. 2010), but the nominal values of the early estimates of  $R_m$  should be cautiously interpreted, as they correspond to inadequate model fits. The estimates for  $C_m$  typically increased slightly immediately after adding MFA, followed by a decrease to a plateau (Fig. 4f). For the 13 cells, we observed no consistent changes of the estimates for  $R_i$  (Fig. 4g) and  $R_s$  (Fig. 4h) during the recording.

Because our recordings were made from single neurons, where we could not independently verify the onset of complete block of gap junctional conductance (in contrast to dual recordings from pairs of coupled neurons; Fig. 2), for each cell we determined by eye the time at which the fitting error and the parameter estimates had stabilized (Fig. 4d). For the cell illustrated in Fig. 4, this occurred approximately 15 min after application of MFA (approximately 25 min after establishing the whole-cell recording configuration), consistent with the results obtained for paired recordings. We used the electrophysiological responses obtained after this time point to obtain a grand average (typically averaged from 1000 - 3000 individual responses) and obtained

the final model parameters from optimization (in NEURON) with this grand average. For the AII amacrine cell illustrated in Fig. 4, this model fitting resulted in  $C_m = 0.86 \mu\text{F} \cdot \text{cm}^{-2}$ ,  $R_i = 223 \Omega \cdot \text{cm}$ ,  $R_m = 43 \text{k}\Omega \cdot \text{cm}^2$  and  $R_s = 16 \text{M}\Omega$ . For all AII amacrine cells analyzed in this manner, the average best-fit parameters were:  $C_m = 0.91 \pm 0.14 \mu\text{F} \cdot \text{cm}^{-2}$ ,  $R_i = 198 \pm 62 \Omega \cdot \text{cm}$ ,  $R_m = 30.2 \pm 8.7 \text{k}\Omega \cdot \text{cm}^2$ , and  $R_s = 25.0 \pm 11.3 \text{M}\Omega$  ( $n = 13$ ; Table 1). The individual best-fit parameters for each of the 13 cells are shown in Table 2 and were used for all subsequent modeling.

*Tables 1 and 2 near here*

In addition to the parameters directly obtained from the model fitting for each cell, we calculated other functionally important properties from the obtained parameters and the reconstructed morphology (Table 1). The membrane time constant ( $\tau_m$ ) was calculated as the product of  $R_m$  and  $C_m$ . The input resistance of the compartmental model was calculated as  $R_{in} = \Delta V / I_{ss}$ , where  $\Delta V$  is the amplitude of the voltage pulse and  $I_{ss}$  is the amplitude of the evoked current response (measured at the end of the 20 ms long voltage pulse). The total membrane capacitance was calculated from  $C_m$  and the total area of the morphologically reconstructed cell (using NEURON's *area* function). In addition, we estimated the relative signal attenuation ( $V_{att}$ ) over the cell for inputs at the cell body at 0, 100, and 1000 Hz (using NEURON's impedance functions).  $V_{att}$  was calculated as the RMS value of the attenuation for the whole cell (cell body and dendrites), averaged by membrane area. Finally, the resting membrane potential ( $V_{rest}$ ) was estimated as  $V_{hold} - (I_{hold} \times R_{in})$ , where  $I_{hold}$  is the average holding current (averaged over 5 ms before onset of the voltage step).

### **Error analysis**

We assessed the accuracy of the obtained model parameters by estimating both random error and systematic error. The random error was estimated by bootstrapping (see Methods; Table 2). With respect to systematic errors, we assumed that their main source is related to errors in the morphological reconstruction. When repeating the

reconstruction of an individual neuron, it is our experience that in general there is little variability of the topology as such, but that there can be some variation in the average diameter of reconstructed segments (cf. Jaeger 2001). Thus, as an estimate of systematic error, we repeated the model fitting for each cell after either increasing or decreasing all diameters by  $0.1 \mu\text{m}$ . To prevent generation of unrealistically thin branches, diameters were not reduced below  $0.1 \mu\text{m}$  (for a detailed discussion, see Zandt et al. 2017). For each parameter, the systematic error was estimated as the average absolute difference between the value obtained from this modified morphology and that obtained for the original morphology. Finally, the total error for a given parameter was calculated as the square root of the sum of the squared individual (random and systematic) errors. For comparison between parameters, the total error for each parameter is reported relative to the mean value of the parameter (Table 1).

From Table 1, it can be seen that for the specific properties of the membrane ( $C_m$ ,  $R_m$ ) and cytoplasm ( $R_i$ ), the total errors were relatively large (approximately 20% for  $C_m$  and  $R_m$  and 35% for  $R_i$ ), due to uncertainty in determining the diameters of the processes of the dendritic tree, consistent with the uncertainty of the estimates for the total area of the membrane (approximately 20%; as determined in NEURON). In contrast, the functional properties of the membrane, e.g. the time constant and input resistance, were obtained with relatively small errors (approximately 1 - 5%).

*Fig. 5 near here*

A systematic difference between the reconstructed and true diameters of the cell processes affects the total membrane area of a morphological reconstruction and thus the specific membrane parameters obtained from model fitting (e.g. Perreault and Raastad 2006; Oltedal et al. 2009). The true diameter refers to the value that would have been measured with no influence from the measurement technique itself. Specifically, a difference between the reconstructed and true area is expected to induce a negative correlation between the fitted values obtained for  $C_m$  and  $R_m$  because they will both be affected by such an error (e.g. Oltedal et al. 2009). When we displayed  $R_m$  vs.  $C_m$  (not shown), we observed a weak, statistically non-significant, negative

correlation ( $R^2 = 0.093$ ) with a slope of  $-20 \pm 18$  ( $\text{k}\Omega \cdot \text{cm}^2$ ) / ( $\mu\text{F} \cdot \text{cm}^{-2}$ ). This suggests that the natural variation of the specific membrane resistance (between cells) is larger than any errors in the total membrane area of the cells introduced during the reconstruction procedure. The theoretical relationships between the magnitude of a difference between the reconstructed and true diameters of a neuronal process and the consequent deviation from the true value of the parameters  $R_i$ ,  $R_m$ ,  $C_m$  and  $\tau_m$ , assuming no other errors, are illustrated in Fig. 5a. For the reconstructed AII amacrine cells, we systematically investigated the relationships between the modal process diameter of a given reconstruction and the estimated membrane properties  $C_m$ ,  $R_m$ ,  $\tau_m$  and  $R_i$  (Fig. 5b-e). The modal diameter has the advantage over the average diameter that it is less influenced by the thick primary dendrite (that is typical of AII amacrine cells; Fig. 1c, d) and was calculated as the mode of the diameters of all reconstruction points of a neuron.

We observed a very strong correlation between the inverse of the modal diameter and  $C_m$  ( $R^2 = 0.403$ ; Fig. 5b). This suggests that a substantial part of the variation in the fitted values for  $C_m$  is caused by deviations in the diameters (and hence area) of the reconstructed processes. Most likely, this is related to the inherent difficulty in tracing thin dendrites with diameters at the resolution limit of light microscopy. However, we found a considerably weaker correlation between the modal diameter and  $R_m$  ( $R^2 = 0.072$ ; Fig. 5c), implying that there is a relatively large natural variation of  $R_m$  between cells. In contrast, no correlation at all was found between the modal diameter and  $\tau_m$  ( $= R_m \times C_m$ ;  $R^2 = 0.00097$ ; Fig. 5d), showing that the relationships of  $R_m$  and  $C_m$  with the average process diameter cancel each other because the fitting procedure successfully compensates for a deviation of the reconstructed membrane area from the true membrane area. Finally, we observed a strong correlation between the (squared) modal diameter and  $R_i$  ( $R^2 = 0.247$ ; Fig. 5e). This is consistent with the estimated error of  $\sim 34\%$  for the fitted value of  $R_i$ , based on simulations where we changed the diameters of the reconstructed processes by a

constant magnitude ( $\pm 0.1 \mu\text{m}$ ) for the compartmental simulations (Table 1). The relatively large variation of specific properties such as  $R_i$  reflects a compensation of the fitting procedure for any systematic over- or underestimation of branch diameters inherent to light-microscopic reconstructions. As a result of this compensation, the functional properties of the cell models, such as signal attenuation, are still obtained with small errors (about 1 - 5%). This is a significant benefit of the combination of electrophysiological recording and morphological imaging from the same cells (cf. Holmes 2010).

*Fig. 6 near here*

### **Estimating the membrane time constant with current-clamp recordings**

As stated above, the membrane time constant ( $\tau_m$ ) can be estimated by calculating it as the product of  $R_m$  and  $C_m$  obtained from the model fitting with voltage-clamp responses. To validate these estimates, we measured  $\tau_m$  directly from current-clamp recordings. Following block of electrical coupling with MFA, we used LFVC recording to keep the average  $V_m$  close to -60 mV (see Methods) and injected short (2 ms) and long (500 ms) pulses of current. Current amplitudes were adjusted such that they evoked membrane potential deflections of approximately  $\pm 2$  to  $\pm 3$  mV. Representative examples of the voltage decay at the end of both short and long pulse stimulation in an AII amacrine cell are illustrated in Fig. 6a. For the short pulses, the intracellular charge redistribution over the cell took place within the first millisecond after the offset of the pulse (Fig. 6b). After that, the decay of the membrane potential was determined by  $\tau_m$  and was very similar to the decay observed after charging the cell with a long pulse (Fig. 6a). The similarity of decay can be optimally observed when the membrane potential is displayed on a logarithmic axis (Fig. 6c).

For five AII amacrine cells, we obtained sufficiently stable recordings to allow a detailed analysis and comparison of  $\tau_m$  estimated with both current-clamp and voltage-clamp recordings. The decay of the membrane potential during the interval from 5 to

200 ms following the offset of the current stimulus was analyzed by curve fitting with a single-exponential function. Fig. 6d and e show representative examples of single-exponential fits to the decay of membrane potential after both short (Fig. 6d) and long (Fig. 6e) positive and negative current pulses. Curve fitting was performed on an average obtained from 100 individual responses and for each cell we obtained 8 - 16 sets of averaged responses (for both short and long pulses). An example is illustrated in Fig. 6f, with estimates of  $\tau_m$  during both voltage-clamp recording (from  $\tau_m = R_m \times C_m$ ) and current-clamp recording (from fitting the decay phase). In the period with voltage-clamp recording, the value for  $\tau_m$  ( $R_m \times C_m$ ) gradually increased from ~10 ms to 20 - 25 ms, reflecting the increasing block of gap junction coupling by MFA. After switching to current clamp, the estimates obtained by curve fitting to the decay of membrane potential responses evoked by applying current pulses were similar to the indirect estimates obtained at the end of the period with voltage-clamp recording. For each cell, the time constants obtained directly from current-clamp responses were averaged and compared with the time constant obtained from  $R_m$  and  $C_m$  estimated by model fitting using the voltage-clamp responses. Whereas there was considerable variability, for each cell the average time constant obtained from current-clamp recording was overall very similar to that obtained from model fitting with voltage-clamp recording, with no systematic deviation (average relative deviation  $1 \pm 12\%$ ;  $n = 5$  cells; Fig. 6g).

*Fig. 7 near here*

### **Passive signal attenuation in AII amacrine cells**

AII amacrine cells are relatively small and it has been argued that they are also electrotonically compact (Vardi and Smith 1996; Schubert and Euler 2010; Cembrowski et al. 2012; Diamond 2017). In general, if a neuron is electrotonically compact, it means that the membrane voltage is approximately constant in space and that the cell can be approximated as a single electrical compartment. Considering a dendritic tree to be electrotonically compact has several implications. First, the location of synaptic or voltage-gated ion channels will be inconsequential with respect to the

electrophysiological response characteristics of the cell. Second, no or only little electrotonic filtering is expected to occur for signals that propagate over the cell. Finally, the voltage control in a voltage-clamp recording is expected to be good and not suffer from "space-clamp" problems. To investigate whether AII amacrine cells are indeed electrotonically compact, we used model simulations to explore these implications in more detail.

To quantify the passive signal transmission characteristics in non-coupled AII amacrine cells, we used the frequency tool in NEURON. This tool is based on the electrotonic transform developed by Carnevale et al. (1995) and calculates the attenuation between the voltage at the site of current injection ( $V_{\text{inject}}$ ) and the voltage at a specific site of interest ( $V_{\text{measure}}$ ). In our simulations, sinusoidal current stimuli were injected at specific locations in the cell, either the soma, a lobular appendage, or the tip of an arboreal dendrite (Fig. 7a). We selected representative sites for current injection at arboreal dendrites and lobular appendages such that their dendritic path lengths to the soma were close to the modal path length to the soma for all the cell's arboreal and lobular dendritic tips, respectively. The stimulus frequency ranged from 1 Hz to 100 kHz and for each frequency the passive signal transmission was characterized by calculating an attenuation factor ( $\Delta V_{\text{att}}$ ) defined as  $1 - (\Delta V_{\text{measure}} / \Delta V_{\text{inject}})$ , effectively normalizing the voltage change at the site of interest by the change at the injection site (e.g. Spruston et al. 1994).

To obtain an overall impression of the signal attenuation in an AII amacrine cell, we coded the degree of attenuation by using a color scale, with red corresponding to no attenuation ( $\Delta V_{\text{measure}} / \Delta V_{\text{inject}} = 1$ ) and black corresponding to complete attenuation ( $\Delta V_{\text{measure}} / \Delta V_{\text{inject}} = 0$ ). Fig. 7a shows an example of the relative membrane potential distribution evoked by injecting sinusoidal current at three different sites (soma, lobular appendage, arboreal dendrite) at two different stimulation frequencies (0, 100 Hz). For low frequency signals (0 Hz) injected at the soma or a lobular appendage, the attenuation was relatively small, but homogeneous over the cell's membrane (Fig. 7a, case 1 and 3). For stimulation at the tip of an arboreal dendrite, the

attenuation increased significantly as a function of distance from the site of injection (Fig. 7a, case 5). For higher-frequency signals (100 Hz) there was stronger attenuation, with the most abrupt attenuation seen for stimulation at the arboreal dendrite (Fig. 7a, case 6). Overall, the largest attenuation occurred for signals generated distally in the dendritic tree and propagating towards the soma. The smallest attenuation occurred for signals generated at the soma and spreading into the dendritic tree.

For quantitative analysis, we plotted the signal transmission ( $\Delta V_{\text{measure}} / \Delta V_{\text{inject}}$ ) as a function of stimulus frequency for the different combinations of injection and measurement sites. The cutoff frequency (-3 dB) was calculated as the stimulus frequency at which the response at the site of interest was attenuated to  $1/\sqrt{2}$  ( $\sim 0.707$ ) of the steady-state response. Fig. 7b shows the response measured at the arboreal dendrite and lobular appendage to stimulation at the soma of the cell illustrated in Fig. 7a. Responses at representative arboreal and lobular dendrites for all 13 cells are illustrated in Fig. 7c and d, respectively. For DC stimulation (0 Hz) at the soma, the transmitted signal was only slightly attenuated at both arboreal and lobular dendrites. For the cell illustrated in Fig. 7a, the DC attenuation towards the arboreal dendrite was 2.9% and the average for all the cells was  $3.5 \pm 2.0\%$  (range 1.5 - 8.3%). The cutoff frequency for the cell illustrated in Fig. 7a was  $\sim 160$  Hz (Fig. 7b) and the average for all the cells was  $250 \pm 120$  Hz (range 110 - 530 Hz; Fig. 7c). The attenuation towards the lobular dendrites was even smaller. For the cell illustrated in Fig. 7a, the DC attenuation was 0.5% and the cutoff frequency was 2.2 kHz (Fig. 7b). The corresponding average values for all 13 cells were  $0.83 \pm 0.82\%$  (range 0.16 - 3.1%) and  $5.1 \pm 6.7$  kHz (range 0.3 - 23 kHz; Fig. 7d). The frequency-dependent attenuation seen here for signals generated at the soma is consistent with the reduced baseline capacitance observed with increasing sine wave frequency in experiments that used capacitance measurements to study exocytosis from AII amacrine cells (Balakrishnan et al. 2015).

The degree of attenuation was much stronger for signals generated in the dendritic tree. The response measured at the soma to stimulation at an arboreal

dendrite or a lobular appendage of the cell in Fig. 7a is illustrated in Fig. 7e. Responses to stimulation at representative arboreal and lobular dendrites for all 13 cells are illustrated in Fig. 7f and g, respectively. When stimulating an arboreal dendrite, the DC response at the soma was notably attenuated compared to the local response in the dendritic tree. For the cell illustrated in Fig. 7a, the degree of attenuation towards the soma was 15% and the average for all the cells was  $26 \pm 11\%$  (range 9 - 43%; Fig. 7f). Notably, only signals up to ~50 Hz were transmitted. For the cell illustrated in Fig. 7a, the cutoff frequency was 30 Hz (Fig. 7e) and the average value for all cells was  $31 \pm 22$  Hz (range 16 - 84 Hz; Fig. 7f). This suggests that high frequency inputs primarily affect the local membrane voltage, with low transmission to the rest of the cell. Compared to signals generated distally at the arboreal dendrites, signals generated at the lobular appendages were less strongly attenuated when transmitted throughout the cell. For the cell illustrated in Fig. 7a, the DC attenuation was 3.2% and the cutoff frequency was 120 Hz (Fig. 7e). The corresponding average values for all the cells were  $9.7 \pm 8.7\%$  (range 1.1 - 35%) and  $130 \pm 200$  Hz (range 22 - 780 Hz; Fig. 7g).

Electrotonic filtering of signals is only relevant if the evoked membrane voltage deflections, occurring at a certain frequency, reach a non-negligible amplitude at the stimulus site. Because the cell membrane behaves as an RC-circuit, high-frequency current inputs will evoke low-amplitude voltage responses. We analyzed this quantitatively by calculating the input impedance ( $Z_{in}$ ) at the three stimulus locations, corresponding to the soma, a lobular appendage, and an arboreal dendrite (Fig. 7h). The voltage response amplitude can be calculated from  $\Delta V_m = Z_{in} \times I_{in}$ , where  $I_{in}$  is the input current. The input resistance (i.e., input impedance at 0 Hz) estimated for current injection in the soma was 2000 M $\Omega$  and the impedance displayed a cutoff frequency of 4.5 Hz (Fig. 7h). For all 13 cells, the average input resistance measured at the soma was  $1600 \pm 500$  M $\Omega$  (range 810 - 2460 M $\Omega$ ) and the cutoff frequency was  $6.5 \pm 1.7$  Hz (range 4.5 - 9.2 Hz; Fig. 7i). Note that the input resistance at the arboreal location remained relatively higher for frequencies up to approximately 1 kHz. This suggests that high-

frequency membrane voltage fluctuations with significant amplitudes can be evoked locally in the arboreal dendrites.

Taken together, these results suggest that signals generated at or close to the soma and the shorter lobular dendrites are transmitted throughout the AII amacrine with relatively low attenuation. In contrast, voltage fluctuations generated in arboreal dendrites at frequencies above ~50 Hz remain to a large extent local, with only low frequency signals transmitted to the rest of the cell. Accordingly, the AII can only be considered to be electrotonically compact when input currents or conductances are slowly changing and located at the soma and/or the shorter lobular dendrites.

*Fig. 8 near here*

The analysis presented above provides a detailed overview of how signals can be transmitted in a passive AII amacrine cell, in particular how the transmission depends on frequency. It provides less information, however, with respect to how the transmission depends on the spatial location of the input in the dendritic tree. To complement this analysis, we generated space plots for single neurons in response to stimulation either at the soma or a location in the dendritic tree. In these space plots (Fig. 8), the calculated response or impedance is plotted as a function of path distance from the soma and points on the same branch are connected by lines. We first examined the local input impedance by measuring the local membrane potential amplitude induced by an injected current. The input impedance was calculated for each segment and normalized to that at the soma. The input impedance at 0 Hz (equal to the input resistance) was relatively homogeneous across the whole cell (Fig. 8a, left; same cell as in Fig. 7). Locally, the same current stimulus can evoke maximally a 30% higher membrane potential deflection when injected at the tips of arboreal dendrites rather than at the soma. At higher frequencies (100 Hz), the regional differences are much more pronounced (Fig. 8a, right) and at the tips of the arboreal dendrites, amplitudes up to ~6 times as large as at the soma can be evoked. We also characterized the signal transmission from the dendritic stimulation site to the soma (Fig. 8b), calculated as the ratio between the signal amplitude at the soma and the signal

amplitude at the stimulation site ( $V_{\text{soma}} / V_{\text{stim}}$ ). It can be seen that signals generated at the tips of the arboreal dendrites (approximately 40 - 60  $\mu\text{m}$  from the soma) have a much larger attenuation than signals generated at the lobular appendages (0 - 30  $\mu\text{m}$  from the soma) when propagating towards the soma (Fig. 8b, left). Increasing the stimulus frequency increased the attenuation for all locations, but the attenuation was still considerably larger for all arboreal dendrites than for lobular dendrites and appendages (Fig. 8b, right). Importantly, this attenuation largely compensates for the corresponding differences in local input impedance (Fig. 8a). This compensation is clear from the transfer impedance ( $Z_{\text{tr}}$ ; equal to the input impedance divided by the signal transmission  $V_{\text{soma}} / V_{\text{stim}}$ ) as calculated between the soma and the locations in the dendritic tree (Fig. 8c). The (normalized) transfer impedance corresponds to the response amplitude at a location in the dendritic tree when the soma is stimulated, which, somewhat counterintuitively, is equal to the response amplitude at the soma when a location in the dendritic tree is stimulated. Both low (0 Hz; Fig. 8c, left) and high (100 Hz; Fig. 8c, right) frequencies were transmitted from the soma to the rest of the cell with relatively low attenuation (<4% and <20%, respectively). Because transfer impedance is a symmetric property, these plots therefore also characterize the signal amplitude evoked at the soma when a location in the dendritic tree is stimulated. Importantly, this demonstrates that a given current stimulus evokes approximately the same membrane depolarization at the soma, irrespective of input location. This phenomenon is explained by the higher local signal amplitude being balanced by a stronger attenuation towards the soma and is referred to as "passive normalization" (Jaffe and Carnevale 1999).

*Fig. 9 near here*

### **Voltage- and space-clamp control during electrophysiological recording of AII amacrine cells**

Our finding that the AII amacrine cannot be characterized as an electrotonically compact neuron has implications for using whole-cell voltage-clamp recording for

studying ion channels in these cells. The extent to which the membrane voltage of a given type of neuron can be controlled experimentally, e.g. in a whole-cell recording, is of considerable practical interest and important when investigating the properties of both ligand- and voltage-gated currents, e.g. voltage-gated  $\text{Na}^+$  currents (Boos et al. 1993), voltage-gated  $\text{Ca}^{2+}$  currents (Habermann et al. 2003), voltage-gated  $\text{K}^+$  currents (Tian et al. 2010; Cembrowski et al. 2012), and spontaneous postsynaptic currents (spPSCs) mediated by glutamate (Veruki et al. 2003) or glycine receptors (Gill et al. 2006). To use our passive models to investigate the degree of voltage control when recording large-amplitude currents, we made the simplifying assumption that the corresponding conductance is homogeneously distributed and activated over the cell. We then added a voltage-insensitive potassium conductance  $g_{\text{K}}$  to the cell membrane (in addition to the leak conductance). The reversal potential ( $E_{\text{K}}$ ) was set to -80 mV and the magnitude varied between 0 and 1  $\text{mS}/\text{cm}^2$ . An ideal voltage clamp (i.e.,  $R_{\text{s}} \sim 0$ ) was inserted at the soma, corresponding to a whole-cell recording. Finally, we set the command potential ( $V_{\text{com}}$ ) to -60, -40, -20 or 0 mV and recorded the resulting voltage-clamp current and membrane voltage distribution in steady state.

For a relatively low conductance and low driving force, the voltage control of the cell was reasonably good. In the example illustrated in Fig. 9a (left),  $g_{\text{K}}$  was set to 0.018  $\text{mS}/\text{cm}^2$  to generate a clamp current of 20 pA (with a voltage-clamp command potential of -40 mV). The maximum deviation of the membrane voltage relative to the command potential was  $\sim 1.5$  mV (corresponding to the location of the most distal branches of the arboreal dendrites). When  $g_{\text{K}}$  was increased (to 0.13  $\text{mS}/\text{cm}^2$ ) to generate a clamp current of 100 pA, the degree of voltage control clearly worsened, with the membrane voltage in large parts of the arboreal dendritic tree deviating more than 4 mV relative to the command potential (Fig. 9a, middle). However, the voltage control of several lobular dendrites was still relatively good. When  $g_{\text{K}}$  was increased even further (to 0.29  $\text{mS}/\text{cm}^2$ ) to generate a clamp current of 200 pA, the entire arboreal dendritic tree deviated more than  $\sim 5$  mV from the command potential, corresponding to a clear escape from voltage clamp (Fig. 9a, right).

When the difference between the pipette command potential and  $E_K$  was relatively small, e.g. at a command potential of -60 mV, the clamp current increased almost linearly with  $g_K$  (Fig. 9b). When the difference between the command potential and  $E_K$  became increasingly larger, the clamp current deviated increasingly from the expected linear relationship, corresponding to increasingly worse voltage control related to a progressive reduction in the driving force for  $I_K$ . To further analyze the degree of escape of the membrane voltage relative to the command potential, we calculated the RMS of the voltage deviation over the dendritic tree ( $\Delta V_{\text{RMS}}$ ). To calculate the average  $\Delta V_{\text{RMS}}$ , the contribution of each segment was weighted by its corresponding membrane area.  $\Delta V_{\text{RMS}}$  increased with increasing  $g_K$  and an increasing difference between the command potential and  $E_K$  (Fig. 9c). We eliminated the explicit representation of  $g_K$  by plotting  $\Delta V_{\text{RMS}}$  as a function of the clamp current, irrespective of  $g_K$  (Fig. 9d). For small currents (<200 pA),  $\Delta V_{\text{RMS}}$  was approximately linearly related to the clamp current (Fig. 9d). This conveniently allowed us to estimate a criterion for adequate steady-state voltage control of the cell based on the clamp current, independent of the command voltage,  $g_K$  or  $E_{\text{rev}}$ . As a reasonable criterion for adequate voltage control, we selected  $\Delta V_{\text{RMS}} < 1$  mV. For the cell illustrated in Fig. 9d, this criterion corresponded to a maximum, steady-state clamp current of 23 pA. The average maximum clamp current (for  $\Delta V_{\text{RMS}} < 1$  mV) for all 13 cells was  $26 \pm 7$  pA (range 16 - 38 pA). For comparison, the average holding current (at  $V_{\text{hold}} = -60$  mV) for the same cells was  $-7.2 \pm 6.4$  pA (range ~0 to ~-20 pA) after blocking the gap junctions. The magnitude of voltage-gated currents that can be evoked in AII amacrine cells is much higher and can reach up to several nA in whole-cell, voltage-clamp experiments (e.g. Boos et al. 1993; Tian et al. 2010). This means that good voltage control cannot be expected for AII amacrine whole-cell, voltage-clamp recordings of steady-state currents with physiologically realistic amplitudes and with non-zero  $R_s$ . In our analysis, we assumed a spatially homogeneous distribution of the conductance. For a heterogeneously distributed conductance, the degree of voltage control will be better if

the conductance density is larger towards and concentrated at the soma and worse if the conductance density is larger towards and concentrated at the arboreal dendrites.

The above analysis focused on the steady-state condition and ignored the consequences of inadequate space-clamp control for the kinetic properties of the recorded currents. However, whole-cell voltage-clamp recording has also been used to record spPSCs in AII amacrine cells, both glutamatergic, excitatory spPSCs (spEPSCs; e.g. Veruki et al. 2003) and glycinergic, inhibitory spPSCs (spIPSCs; Gill et al. 2006). With perfect voltage clamp, the waveform of a spPSC will correspond directly to that of the underlying conductance waveform at the synapse. Because recorded spPSCs can display very fast kinetics, it is likely that they are distorted relative to the true synaptic conductances generated in the dendritic tree, both with respect to amplitude and kinetics. To explore this quantitatively, we performed simulations of somatic whole-cell voltage-clamp recordings where a conductance waveform corresponding to glutamatergic spEPSCs recorded in AII amacrine cells (Veruki et al. 2003; see Materials and methods) was injected at different locations in an AII dendritic tree, mimicking synaptic input at a lobular appendage close to the apical dendrite (Fig. 9a; arrow labeled "L") or at the distal tip of an arboreal dendrite (Fig. 9a; arrow labeled "A"). The simulations were repeated for a series of values for  $R_s$ , ranging from  $\sim 0$  to 50 M $\Omega$  (with increments of 5 M $\Omega$ ), as well as a final trial with 100 M $\Omega$ . With input at the distal arboreal dendrite (Fig. 9a), arguably corresponding to a worst-case space-clamp condition, the voltage-clamp currents recorded at the soma were markedly distorted relative to the current obtained with the same conductance waveform and perfect voltage clamp (Fig. 9e). Even in the condition with  $R_s$  of  $\sim 0$  or 1 M $\Omega$ , the peak amplitude of the current was reduced to  $\sim 50\%$  of the theoretical amplitude and with increasing  $R_s$ , the peak amplitude gradually decreased to  $\sim 30\%$  for 50 M $\Omega$  ( $\sim 25\%$  for 100 M $\Omega$ ; Fig. 9e). In parallel with the amplitude reduction, increasing  $R_s$  led to increasing delay to the time of the peak amplitude and increasing widening of the current waveform recorded at the soma (Fig. 9e, f). Even with  $R_s$  of  $\sim 0$  or 1 M $\Omega$ , the width (measured as full width at half-maximum) was  $\sim 200\%$  of the theoretical width

and with increasing  $R_s$ , the width gradually increased to ~300% for 50 M $\Omega$  (~380% for 100 M $\Omega$ ; Fig. 9f).

With input at the proximal lobular dendrite (Fig. 9a), the voltage-clamp control was markedly better and the currents recorded at the soma were much less distorted relative to the current obtained with perfect voltage clamp (Fig. 9g). In the condition with  $R_s$  of ~0 or 1 M $\Omega$ , the peak amplitude of the current was reduced to ~80% of the theoretical amplitude and with increasing  $R_s$ , the peak amplitude gradually decreased to ~45% for 50 M $\Omega$  (~30% for 100 M $\Omega$ ; Fig. 9g). Compared to synaptic input at a distal arboreal dendrite, the widening of the current waveforms recorded at the soma was considerably less for the proximal lobular input (Fig. 9g, h). With  $R_s$  of ~0 or 1 M $\Omega$ , the width was ~120% of the theoretical width and with increasing  $R_s$ , the width gradually increased to ~215% for 50 M $\Omega$  (~300% for 100 M $\Omega$ ; Fig. 9h). Similar results were obtained for five other cells tested in the same way. The extent of amplitude reduction and temporal distortion displayed some variability between cells, but for each cell there was a clear difference between the waveforms obtained for proximal (lobular) and distal (arboreal) locations.

## Discussion

A major motivation for morphological reconstructions of neurons with arborising dendritic trees is to perform computational modeling and simulations of signal integration and propagation using realistic geometries (e.g. Koch 1999).

Compartmental models with a high degree of biological realism can be of crucial importance for *in silico* computational studies of signal integration and processing in single neurons, including amacrine cells in the mammalian retina (e.g. Stincic et al. 2016; Vlasits et al. 2016). Neuronal function can be strongly influenced by the dendritic tree morphology (e.g. Mainen and Sejnowski 1996; Schmidt-Hieber et al. 2007) and computer simulations based on accurate reconstruction of neuronal morphology and electrophysiological recordings are considered necessary to understand the underlying mechanisms of signal integration (Koch 1999; De Schutter and Steuber 2001; De

Schutter and van Geit 2010). In this study we used a combination of MPE microscopic imaging and electrophysiological recording of AII amacrine cells in rat retinal slices to obtain correlated morphological and physiological data to determine the passive membrane properties of these cells and develop morphologically realistic computational models. Subsequently, we used these compartmental models to study passive signal transmission in AII amacrine cells and to examine their electrotonic structure. A major conclusion from our study is that despite the relatively small physical size of AII amacrine cells, there is significant, frequency-dependent attenuation of signal transmission in these cells, and they cannot be characterized as electrotonically compact. In addition, we examined the degree of voltage control during whole-cell voltage-clamp recording of these cells. For steady-state currents, we found that good control is only obtained for current amplitudes less than approximately 20 - 40 pA. For transient conductances, imperfect voltage-clamp control will considerably distort both amplitude and kinetics of the resulting currents.

### **Compartmental models of gap junction-coupled neurons**

Our approach of simultaneously acquiring fluorescent images and electrophysiological responses during an experiment has several advantages compared to an alternative approach based on filling cells with non-fluorescent tracers such as biocytin and Neurobiotin (Horikawa and Armstrong 1988; Kita and Armstrong 1991). First, when recording from gap junction-coupled neurons, it is problematic that these tracers are gap junction-permeable such that there is a real risk of obtaining the morphology of a more extensive structure than that corresponding to the single cell recorded from. In previous work from our laboratory (Veruki et al. 2010), we experienced that limiting the recording time, in order to minimize the time for the tracer to diffuse to coupled cells, resulted in suboptimal filling of thin and distal processes of the neuron from which the recording was made (discussed in Zandt et al. 2017). MPE microscopic imaging during electrophysiological recording also has the advantage that the cellular morphology is unaffected by potential shrinkage that often takes place during

processing and fixation of the tissue (Jaeger 2001; Jacobs et al. 2010). Finally, the current approach allowed us to obtain morphological reconstructions without removing the recording pipette, thereby avoiding the risk of damaging or removing the cell body. This is a particular advantage for small cells like AII amacrine cells where the cell body can constitute a relatively large fraction of the total membrane area ( $10.9 \pm 4.8\%$ ,  $n = 43$  cells; data for cells analyzed in Zandt et al. 2017).

In our study, we used MFA to block gap junction channels and functionally uncouple AII amacrine cells from their coupled neighbors, i.e., ON-cone bipolar cells and other AII amacrine cells. The effectiveness of MFA to completely block the electrical coupling, measured as the junction conductance in simultaneous, dual recording of coupled cells, has been demonstrated previously for coupling between both AII amacrine cells and ON-cone bipolars and between AII amacrine cells (Veruki and Hartveit 2009) and was verified for the recording conditions used in the current study. This approach is similar to that used by Szoboszlay et al. (2016) for gap junction-coupled cerebellar Golgi cells. From the outcome of these two studies, it seems that the use of MFA or a closely related blocker must be considered mandatory when developing accurate compartmental models of gap junction-coupled neurons.

Previous studies from our laboratory suggested that MFA does not influence the passive membrane and cytoplasm properties of AII amacrine cells (Veruki and Hartveit 2009; Veruki et al. 2010). For the present study, we ensured that the responses used for compartmental model fitting were passive and linear. Whereas it is impossible to prove incontrovertibly that MFA does not have any additional influence on membrane properties of AII amacrine cells, it is difficult to envisage an alternative approach that would not itself be hampered by equal or even larger uncertainty. First, it was essentially impossible to obtain a good fit of the current responses of the models to the physiological recordings obtained before and during onset of the action of MFA, suggesting that the physiologically recorded responses are markedly influenced by the electrical coupling. Second, whereas an alternative strategy could be to record from AII amacrine cells in the retina of genetically modified mice that lack Cx36 (the connexin

involved in gap junction coupling of both AII amacrine and ON-cone bipolar cells), there is evidence that tracer coupling may not be completely abolished in Cx36 knockout mice (Deans et al. 2002), potentially consistent with the suggestion that coupling between AII amacrine could involve additional connexins (Meyer et al. 2016), or that compensatory mechanisms in knock-out animals could be triggered and influence expression of other connexins.

### **Accuracy of compartmental models of AII amacrine cells**

In this study, we obtained correlated electrophysiological and morphological data from the same cells. This is a prerequisite for constructing high-quality compartmental models and our error analysis suggested that the functional properties were obtained with very small errors (1 - 5%), even though the errors for specific membrane and cytoplasm properties could be considerably larger. During the model fitting, we used parameter search routines to find optimal values for  $R_i$  (specific cytoplasmic resistivity),  $R_m$  (specific membrane resistance) and  $C_m$  (specific membrane capacitance). The accuracy of the estimates for these parameters will depend on several factors, including the choice of electrophysiological recording mode, i.e., current-clamp or voltage-clamp. Arguments have been presented in favour of either mode (see e.g. Major 2001; Jackson 2006). The most important argument favouring the choice of current-clamp recording is that, at least in theory, it is possible to carefully adjust the bridge balance of the recording amplifier such that  $R_s$  is effectively eliminated and can be set to zero during the subsequent model fitting. Because it can be very difficult to obtain perfect compensation, as is ideally required when the same pipette is used for both voltage recording and current injection, an alternative approach is to use separate electrodes for current injection and voltage recording (Schmidt-Hieber et al. 2007; Nörenberg et al. 2010). Because no current flows across the  $R_s$  of the pipette only used for voltage recording, it should be possible to record the true voltage without the error related to the voltage drop caused by current flowing across  $R_s$  (as long as the recording pipette capacitance is carefully compensated to counteract low-pass filtering

of fast voltage signals by the combination of  $R_s$  and the pipette capacitance). We have so far had limited success with the dual-electrode recording technique for AII amacrine cells, both because of the small cell size and the added difficulty of maintaining such recordings for the extended periods necessary to obtain complete block of electrical coupling with MFA. An additional argument in favour of the dual (somatic) current-clamp recording technique, compared to single-electrode recording, is that it facilitates accurate measurement of the fast charge redistribution observed with short current pulse stimuli, which is essential for constraining estimates of  $R_i$  (Nörenberg et al. 2010). From our results, it seems that voltage-clamp recording with the pipettes used here (and consequent  $R_s$  values) was adequate to capture the fast charge redistribution. Even in some of our current-clamp recordings, we seem to have captured the time course of the fast charge redistribution.

When the electrophysiological recording is done in voltage-clamp mode, it is desirable to either have independent knowledge of  $R_s$  (and fix  $R_s$  to this value during model fitting) or fully compensate it, as even small errors in the value of  $R_s$  can lead to large errors in the estimate for  $R_i$  (Perreault and Raastad 2006). Neither alternative is very realistic, however, as it can be quite difficult to obtain accurate estimates of  $R_s$  and to achieve full compensation of  $R_s$ , i.e., effectively reduce it to zero. The best solution is to include  $R_s$  as a free parameter in the direct fitting of the current responses of the morphological models (see Perreault and Raastad 2006). With the exception of a few cells, this procedure resulted in realistic values for  $R_s$ . For two cells where the estimate for  $R_s$  was unrealistically low ( $< R_{\text{pip}} \times 2$ ),  $R_s$  was constrained to be larger than  $R_{\text{pip}} \times 2$  during model fitting.

In addition to the electrophysiological data, the accuracy of a compartmental model is also strongly influenced by the light microscopic imaging. For quantitative morphological reconstruction, it is problematic when the diameters of the thinnest processes are below the resolution limit of light microscopy (Jaeger 2001; Jacobs et al. 2010), as is the case for AII amacrine cells (see Zandt et al. 2017 for a detailed discussion). For investigations that aim to combine electrophysiological recording and

morphological imaging from the same cells (Holmes 2010), it is currently unrealistic to perform morphological reconstruction by electron microscopy that would provide the ultimate resolution. Of the currently available techniques for super-resolution (diffraction-unlimited) light microscopy, two-photon stimulated-emission depletion (STED) microscopy (Ding et al. 2009) can be combined with electrophysiological recording, is adequate for deep-tissue, volumetric imaging of fluorescent neurons in live brain slices and might be able to resolve even the thinnest processes of AII amacrine cells.

### **The membrane time constant ( $\tau_m$ ) of AII amacrine cells and the influence of electrical coupling**

The membrane time constant is given by the product of  $R_m$  and  $C_m$  and has traditionally been considered an important determinant of the integrative properties of a neuron (see Koch et al. 1996, for a detailed discussion). Despite the ambiguity of the functional meaning of  $\tau_m$  in the context of local dendritic integration (Koch et al. 1996), it is nevertheless important to evaluate the accuracy of the estimated value of  $\tau_m$  for a given compartmental model. For voltage-clamp recording, as employed in our study, only an indirect estimate of  $\tau_m$ , from the best-fit values of  $R_m$  and  $C_m$ , can be made. When we compared the indirect estimate of  $\tau_m$  with direct estimates from current-clamp recording, the average values were very similar (after block of electrical coupling). The average  $\tau_m$  was ~27 ms (range 18 - 38 ms) which is very similar to membrane time constants measured in other types of neurons with the tight-seal, whole-cell recording technique (see Koch et al. 1996 and Koch 1999 for detailed reviews).

The slow kinetics of the block of electrical coupling by MFA favoured repeated sampling of electrophysiological responses in parallel with the gradual reduction of coupling. With the caveat that the (indirect) estimates of  $\tau_m$  during this initial period were obtained from suboptimal model fits, blocking electrical coupling was

accompanied by a corresponding, gradual increase of the value for  $\tau_m$ . Qualitatively, this change is expected, as block of electrical coupling increases the effective value of  $R_m$ . This will influence the integrative properties of AII amacrine cells and is of particular interest because there is evidence that the strength of electrical coupling is modulated as a mechanism of post-receptoral light adaptation in the retina (Bloomfield and Völgyi 2004; Kothmann et al. 2012). It will be interesting to explore the influence of gap junction coupling on the integrative properties of AII amacrine cells using the compartmental models obtained in the current study.

### **Experimental estimates of cytoplasmic resistivity ( $R_i$ )**

We obtained values for  $R_i$  over a fairly wide range (80 - 280  $\Omega \cdot \text{cm}$ ). To some extent, this variability can be explained by uncertainty in the diameters of the reconstructed processes. We used simulations to demonstrate that a systematic difference between the true and the reconstructed diameters of 0.1  $\mu\text{m}$  will change the estimated value of  $R_i$  by about 34% (Table 1). In agreement with this, the estimated values of  $R_i$  show a positive correlation with the (squared) modal diameter of the processes of the reconstructed cells (Fig. 5e). For  $R_i$ , the average value ( $\sim 200 \Omega \cdot \text{cm}$ ) and range ( $\sim 80$  to  $\sim 280 \Omega \cdot \text{cm}$ ) are very similar to estimates for a variety of different neurons obtained with whole-cell recording (Koch et al. 1996; Koch 1999). In a recent study (Szoboszlay et al. 2016), however, it was argued that the high values of  $R_i$  reported in a number of studies (100 - 200  $\Omega \cdot \text{cm}$ ) could be overestimations of the actual values, caused by the presence of (unblocked) gap junction coupling between neurons. The average value for AII amacrine cells ( $\sim 200 \Omega \cdot \text{cm}$ ) is somewhat in the high range of values reported for  $R_i$ , but cannot be explained by the presence of gap junction coupling, as we used MFA to pharmacologically block gap junctions. There are also examples of relatively high estimates of  $R_i$ , e.g. 194  $\Omega \cdot \text{cm}$  for hippocampal dentate gyrus granule cells (Schmidt-Hieber et al. 2007), 140 - 170  $\Omega \cdot \text{cm}$  for layer 2/3 cortical pyramidal cells (Trevelyan and Jack 2002), 139 - 218  $\Omega \cdot \text{cm}$  for CA1 pyramidal cells (Golding et al. 2005), and 170 -

340  $\Omega \cdot \text{cm}$  for CA3 pyramidal cells (Major et al. 1994), that are unlikely to be explained by gap junction coupling. However, two factors probably influenced our estimates of  $R_i$ . The first, as mentioned above, is the uncertainty in the diameters of the reconstructed processes. If we assume that the true value for the specific capacitance ( $C_m$ ) is 1.0  $\mu\text{F} \cdot \text{cm}^{-2}$  (cf. Hille 2001), our estimate of 0.9  $\mu\text{F} \cdot \text{cm}^{-2}$  does indeed suggest that the diameters were overestimated by ~10 % (on average). This would also result in an overestimation of  $R_i$  by ~20%. The second factor that is likely to have influenced our estimate of  $R_i$ , is that our recordings were performed at ~25°C, where the resistivity of the intracellular solution is ~25% higher than at 35°C, assuming a  $Q_{10}$  temperature coefficient (the experimentally determined change for a 10°C difference in temperature) of 0.8 for the resistivity (Trevelyan and Jack 2002). If we correct for both these factors, we obtain an average value of  $R_i$  of ~130  $\Omega \cdot \text{cm}$ , which is considerably closer to the value obtained for cerebellar Golgi cells (92  $\Omega \cdot \text{cm}$ ; 32 - 36°C) by Szoboszlay et al. (2016).

### **Influence of temperature**

There is evidence that not only  $R_i$ , but other passive membrane properties as well, are influenced by temperature. In our study, all electrophysiological recordings were performed at a temperature between 24 and 25°C and we did not attempt to investigate the influence of temperature on the estimates for passive membrane properties. In addition to  $R_i$  (discussed above), Trevelyan & Jack (2002) obtained estimates of  $C_m$  and  $R_m$  before and after cooling from ~36 to ~26°C. As expected,  $C_m$  displayed very low sensitivity to temperature ( $Q_{10} \sim 0.96$ ). For the total membrane conductance they found a  $Q_{10}$  of 1.97. In a study of CA1 pyramidal neurons, Thompson et al. (1985) found a  $Q_{10}$  of 0.6 - 0.75 for the input resistance, corresponding to a  $Q_{10}$  of 1.33 - 1.67 for input conductance which is somewhat lower than the value reported by Trevelyan & Jack (2002) for total membrane conductance. On the other hand, Doll et al. (1993) found a  $Q_{10}$  of 1.9 for the input conductance of pyramidal neurons, similar to the

result of Trevelyan & Jack (2002). For the experimental measurements of the  $Q_{10}$  for the membrane conductance, the lowest values ( $\sim 1.3$ ) are similar to the  $Q_{10}$  for  $R_i$  and difficult to explain, but the highest values ( $\sim 2.0$ ) are similar to the  $Q_{10}$  for the time constants of activation and inactivation of voltage-gated ion channels (e.g. Destexhe & Huguenard, 2010), rate coefficients of gating of ion channels, and many enzyme reactions (Hille, 2001). When it is relevant and necessary to perform computational simulations at higher temperatures, it should be fairly straightforward to correct the estimates for  $R_i$  and  $R_m$  obtained in the present study (at 24 - 25°C) with the corresponding  $Q_{10}$  values obtained by Trevelyan & Jack (2002). Computational simulations of synaptic inputs at physiological temperatures will also need to take into account the effects temperature on the kinetics and conductance of synaptic ion channels. For AII amacrine cells, our laboratory has previously provided estimates for the  $Q_{10}$  values for  $\tau_{\text{decay}}$ , 10-90% rise time, and peak amplitude of spEPSCs (Veruki et al. 2003, see also Hartveit et al. 2018).

### **Passive signal transmission and electrotonic properties of AII amacrine cells**

To understand signal transmission and transformation in AII amacrine cells, it is necessary to analyze, at a quantitative level, the interaction between morphology, passive membrane properties, and voltage- and ligand-gated conductances, including the spatial and temporal patterns of activation of the synaptic inputs. In the current study, we used the compartmental models to study electrotonic signal transmission in AII amacrine cells.

An important result of our study is that, contrary to previous suggestions (Vardi and Smith, 1996; Schubert and Euler 2010; Cembrowski et al. 2012; Diamond 2017), the AII amacrine cell cannot be characterized as electrotonically compact. However, using both a reduced (3-compartment) model and a simplified, morphologically inspired model to study the spiking properties of mouse AII amacrine cells, it was recently argued that a specialized AIS-like process (Wu et al. 2011) is electrotonically remote from the rest of the cell (Cembrowski et al. 2012; Choi et al.

2014). Whereas we agree that an AIS-like process appears morphologically distinct in many cells, we believe that it is misleading to markedly separate it from all other processes of the cell with respect to the overall electrotonic structure. First, although there are examples of AII amacrine cells, both in mouse and rat retina, where the presumed AIS-like process is particularly long compared to other lobular dendrites, this is not always the case. Some AII cells, with normal spiking mediated by voltage-gated  $I_{Na}$ , do not display a lobular dendrite that is obviously morphologically distinct (at the light microscopic level) from other processes (this study; Zandt et al. 2017). Second, even in cases where a strong candidate for an AIS-like process can be identified, its length does not set it apart compared to arboreal dendrites of the same cells. Importantly, with simulations of signal transmission using morphologically realistic compartmental models of AII amacrine cells, we observed significant frequency-dependent attenuation, most pronounced for transmission of signals generated at the tips of arboreal dendrites and spreading towards the cell body and lobular dendrites.

Our computational modeling of signal transmission in AII amacrines was based on using compartmental models that correspond to completely uncoupled cells and it might be argued that this is unphysiological. Whereas we believe that the influence of electrical coupling on synaptic integration must be examined in detail in future studies, we would like to argue that the results for the uncoupled condition serve as a useful reference for other models with varying strength and extent of electrical coupling. In addition, there is strong evidence that the strength of coupling is strongest under high scotopic / low mesopic conditions, with major reduction of coupling during both strong dark and light adaptation, such that AIIs seem essentially uncoupled in absolute darkness (Bloomfield and Völgyi 2004; for a recent review, see Diamond 2017). Irrespective of whether complete uncoupling can occur *in vivo*, opening of gap junction channels will effectively increase the membrane conductance (similar to activation of voltage-gated ion channels). This will increase signal attenuation across the dendritic tree of the cell, and further decrease the degree of electrotonic compactness of the cell.

The electrotonic non-compactness of AII amacrine cells found in the present study has important consequences for the interpretation of voltage-clamp data obtained for these cells. First, it is clear that with realistic current amplitudes of voltage-gated  $K^+$  channels, there will be substantial voltage escape in the dendritic tree, thus voltage-clamp recording of such currents (Boos et al. 1993; Tian et al. 2010) must be interpreted with considerable caution, in particular when the relevant channels are located far from the soma. Even in cases where the primary focus is on the steady-state (as opposed to the kinetic) properties of the currents, it is wrong to assume that linear compensation for the voltage drop across  $R_s$  (between recording pipette and soma) will correctly adjust the current amplitudes (cf. Boos et al. 1993), as this procedure implicitly assumes an exclusive somatic location of the corresponding channels. The situation is more advantageous for studies of voltage-gated  $Ca^{2+}$  channels, as the relevant current amplitudes are considerably smaller compared to voltage-gated  $K^+$  currents and the primary location is in the lobular dendrites, closer to the soma and the recording pipette (Habermann et al. 2003). For voltage-gated  $Na^+$  channels, expressed at the AIS-like process (Wu et al. 2011; Cembrowski et al. 2012), their fast kinetics and typically distal location mean that adequate voltage-clamp control is essentially impossible, as is clearly illustrated by the characteristic action currents that can be recorded in AII amacrine cells (Fig. 1b). The compartmental models obtained in the current study offer the possibility to explore quantitatively the recording errors of both transient and steady-state properties for conductances inserted at discrete locations in the dendritic tree. Although experimentally demanding, it might be possible to combine voltage-clamp recording and compartmental modeling of the same cell and use the correlated data to estimate the expected errors and subsequently vary the model properties iteratively until the simulated currents match the experimentally recorded currents (see Schaefer et al. 2003 for an example using dendritic recordings). An additional requirement for a successful outcome is independent knowledge of the location of the ion channels in the dendritic tree.

For recordings of spontaneous postsynaptic currents (spPSCs) with very fast kinetics, e.g. glutamatergic spEPSCs, the lack of space-clamp control across the dendritic tree will lead to distortion of currents recorded with a somatic whole-cell voltage clamp, evident as both amplitude reduction and temporal widening. In our simulations of whole-cell, voltage-clamp recording of currents evoked by synaptic conductance waveforms injected at different locations in the dendritic tree of an AII amacrine, we used a waveform generated from glutamatergic spEPSCs recorded in AII amacrine cells (Veruki et al. 2003). This means that whereas the different current waveforms observed for proximal (lobular) and distal (arboreal) synaptic inputs illustrate differential filtering as a function of synaptic location in the dendritic tree, the kinetic properties of the simulated currents cannot be directly compared with those from the physiological recordings, as the recorded spEPSCs have been distorted by electrotonic filtering and imperfect space-clamp control. An important consequence from our simulations, however, is that the kinetically fastest spEPSCs obtained in whole-cell, voltage-clamp recording from AII amacrine cells may originate predominantly from OFF-cone bipolar cells contacting the lobular dendrites, whereas rod bipolar cells contacting the arboreal dendrites may give rise to kinetically slower spEPSCs. It is possible that combined investigations with physiological recording of spEPSCs and compartmental modeling of the same AII amacrine cells will permit "reverse engineering" the true synaptic conductance waveforms giving rise to the different somatically recorded current waveforms, but this will require determining the spatial origin of specific spEPSCs. An alternative strategy can be to circumvent synaptic release and activate glutamate receptors at discrete locations in the dendritic tree using multi-photon uncaging.

### **Signal transmission and integration in AII amacrine cells**

Specific chemical and electrical synaptic inputs and outputs are segregated to different regions of the AII amacrine dendritic tree. When synaptic inputs and outputs are located in close proximity (e.g. chemical synaptic input from rod bipolar cells and

electrical synapses with other AII cells and ON-cone bipolar cells), it is likely that there is substantial signal transfer. For neurons with very thin dendrites, like AII amacrines, electrophysiological recording directly from the dendrites is prohibitively difficult, but morphologically realistic compartmental models enable an alternative approach with *in silico* exploration of local synaptic integration in different parts of the dendritic tree (e.g. Abrahamsson et al. 2012; Vervaeke et al. 2012). When synaptic inputs and outputs are located further away from each other (e.g. chemical synaptic input from rod bipolar cells at the arboreal dendrites and chemical synaptic output to axon terminals of OFF-cone bipolar cells at the lobular dendrites), it is unclear whether and to which extent inputs are integrated and transferred between different subcellular regions of the AII dendritic tree. Although there is evidence that rod bipolar cell excitatory input at the arboreal dendrites can be transmitted to and evoke glycine release from the lobular dendrites (Manookin et al. 2008; Murphy and Rieke 2008; Tian et al. 2010; Balakrishnan et al. 2015), the evidence is indirect and does not by itself provide quantitative information about the transfer efficacy and extent of attenuation. In the light of recent evidence for the extensive and multifunctional connectivity of AII amacrines (Marc et al. 2014), it has also become clear that physiological responses cannot be interpreted in the light of just a few possible connecting pathways. Hopefully, a combination of computational studies with multicompartmental models and simultaneous, multi-electrode recordings from different neuronal elements of the relevant microcircuits will provide answers to these questions.

## References

- Abrahamsson T, Cathala L, Matsui K, Shigemoto R, DiGregorio DA (2012) Thin dendrites of cerebellar interneurons confer sublinear synaptic integration and a gradient of short-term plasticity. *Neuron* 73:1159-1172
- Balakrishnan V, Puthussery T, Kim M-H, Taylor WR, von Gersdorff H (2015) Synaptic vesicle exocytosis at the dendritic lobules of an inhibitory interneuron in the mammalian retina. *Neuron* 87:563-575
- Bloomfield SA, Völgyi B (2004) Function and plasticity of homologous coupling between AII amacrine cells. *Vision Res* 44:3297-3306
- Boos R, Schneider H, Wässle H (1993) Voltage- and transmitter-gated currents of AII-amacrine cells in a slice preparation of the rat retina. *J Neurosci* 13:2874-2888
- Brent, RP (1973) A new algorithm for minimizing a function of several variables without calculating derivatives. In: *Algorithms for Minimization without Derivatives*. Prentice Hall, Englewood Cliffs, pp. 116-167
- Cajal SRy (1893) *La rétine des vertébrés*. *La Cellule* 9:119-255
- Cajal SRy (1909) *Histologie du Système Nerveux de l'Homme et des Vertébrés*, Vol. I. Maloine, Paris
- Cajal SRy (1911) *Histologie du Système Nerveux de l'Homme et des Vertébrés*, Vol. II. Maloine, Paris
- Carnevale NT, Hines ML (2006) *The NEURON Book*. Cambridge University Press, Cambridge
- Carnevale NT, Tsai KY, Claiborne BJ, Brown TH (1995) The electrotonic transformation: a tool for relating neuronal form to function. In: Tesauro G, Touretzky DS, Leen TK (eds) *Advances in Neural Information Processing Systems*, vol. 7. MIT Press, Cambridge, pp. 69-76
- Castilho Á, Ambrósio AF, Hartveit E, Veruki ML (2015) Disruption of a neural microcircuit in the rod pathway of the mammalian retina by diabetes mellitus. *J Neurosci* 35:5422-5433

- Cembrowski MS, Logan SM, Tian M, Jia L, Li W, Kath WL, Rieke H, Singer JH (2012) The mechanisms of repetitive spike generation in an axonless retinal interneuron. *Cell Rep* 1:155-166
- Choi H, Zhang L, Cembrowski MS, Sabottke CF, Markowitz AL, Butts DA, Kath WL, Singer JH, Rieke H (2014) Intrinsic bursting of AII amacrine cells underlies oscillations in the rd1 mouse retina. *J Neurophysiol* 112:1491-1504
- Clements JD, Redman SJ (1989) Cable properties of cat spinal motoneurons measured by combining voltage clamp, current clamp and intracellular staining. *J Physiol* 409:63-87
- Deans MR, Völgyi B, Goodenough DA, Bloomfield SA, Paul DL (2002) Connexin36 is essential for transmission of rod-mediated visual signals in the mammalian retina. *Neuron* 36:703-712
- De Schutter E, Steuber V (2001) Modeling simplex and complex active neurons. In: De Schutter E (ed) *Computational Neuroscience: Realistic Modeling for Experimentalists*. CRC Press, Boca Raton, pp. 233-257
- De Schutter E, van Geit W (2010) Modeling complex neurons. In: De Schutter E (ed) *Computational Modeling Methods for Neuroscientists*. MIT Press, Cambridge, pp. 259-283
- Destexhe A, Huguenard JR (2010) Modeling voltage-dependent channels. In: De Schutter E (ed) *Computational Modeling Methods for Neuroscientists*. MIT Press, Cambridge, pp. 107-137
- Diamond JS (2017) Inhibitory interneurons in the retina: Types, circuitry, and function. *Annu Rev Vis Sci* 3:1-24
- Ding JB, Takasaki KT, Sabatini BL (2009) Supraresolution imaging in brain slices using stimulated-emission depletion two-photon laser scanning microscopy. *Neuron* 63:429-437
- Doll CJ, Hochachka PW, Reiner PB (1993) Reduced ionic conductance in turtle brain. *Am J Physiol* 265:R929-R933

- Gill SB, Veruki ML, Hartveit E (2006) Functional properties of spontaneous IPSCs and glycine receptors in rod amacrine (AII) cells in the rat retina. *J Physiol* 575:739-759.
- Golding NL, Mickus TJ, Katz Y, Kath WL, Spruston N (2005) Factors mediating powerful voltage attenuation along CA1 pyramidal neuron dendrites. *J Physiol* 568:69-82
- Habermann CJ, O'Brien BJ, Wässle H, Protti DA (2003) AII amacrine cells express L-type calcium channels at their output synapses. *J Neurosci* 23:6904-6913
- Hampson ECGM, Vaney DI, Weiler R (1992) Dopaminergic modulation of gap junction permeability between amacrine cells in mammalian retina. *J Neurosci* 12:4911-4922
- Hartveit E, Veruki ML (2010) Accurate measurement of junctional conductance between electrically coupled cells with dual whole-cell voltage-clamp under conditions of high series resistance. *J Neurosci Meth* 187:13-25
- Hartveit E, Veruki ML (2012) Electrical synapses between AII amacrine cells in the retina: Function and modulation. *Brain Res* 1487:160-172
- Hartveit E, Zandt B-J, Madsen E, Castilho Á, Mørkve SH, Veruki ML (2018) AMPA receptors at ribbon synapses in the mammalian retina: kinetic models and molecular identity. *Brain Struct Funct* 223:769-804
- Helmstaedter M, Briggman KL, Turaga SC, Jain V, Seung HS, Denk W (2013) Connectomic reconstruction of the inner plexiform layer in the mouse retina. *Nature* 500:168-174
- Hille B (2001) *Ion channels of excitable membranes*, 3rd edn. Sinauer, Sunderland
- Holmes WR (2010) Passive cable modeling. In: De Schutter E (ed) *Computational Modeling Methods for Neuroscientists*. MIT Press, Cambridge, MA, pp. 233-258
- Horikawa K, Armstrong WE (1988) A versatile means of intracellular labeling: injection of biocytin and its detection with avidin conjugates. *J Neurosci Meth* 25:1-11
- Jackson MB (2006) *Molecular and Cellular Biophysics*. Cambridge University Press, Cambridge

- Jacobs G, Claiborne B, Harris K (2010) Reconstruction of neuronal morphology. In: De Schutter E (ed) *Computational Modeling Methods for Neuroscientists*. MIT Press, Cambridge, pp. 187-210
- Jaeger D (2001) Accurate reconstruction of neuronal morphology. In: De Schutter E (ed) *Computational Neuroscience: Realistic Modeling for Experimentalists*. CRC Press, Boca Raton, pp. 159-178
- Jaffe DB, Carnevale NT (1999) Passive normalization of synaptic integration influenced by dendritic architecture. *J Neurophysiol* 82:3268-3285
- Kita H, Armstrong W (1991) A biotin-containing compound N-(2-aminoethyl)biotinamide for intracellular labeling and neuronal tracing studies: comparison with biocytin. *J Neurosci Meth* 37:141-150
- Koch C (1999) *Biophysics of Computation: Information Processing in Single Neurons*. Oxford University Press, New York
- Koch C, Rapp M, Segev I (1996) A brief history of time (constants). *Cereb Cortex* 6:93-101
- Kolb H, Famiglietti EV (1974) Rod and cone pathways in the inner plexiform layer of cat retina. *Science* 186:47-49
- Kole MHP, Stuart GJ (2012) Signal processing in the axon initial segment. *Neuron* 73:235-247
- Kothmann WW, Trexler EB, Whitaker CM, Li W, Massey SC, O'Brien J (2012) Nonsynaptic NMDA receptors mediate activity-dependent plasticity of gap junctional coupling in the AII amacrine cell network. *J Neurosci* 32:6747-6759
- Mainen ZF, Sejnowski TJ (1996) Influence of dendritic structure on firing pattern in model neocortical neurons. *Nature* 382:363-366
- Major G (2001) Passive cable modeling - a practical introduction. In: De Schutter E (ed) *Computational Neuroscience: Realistic Modeling for Experimentalists*. CRC Press, Boca Raton, pp. 209-232

- Major G, Larkman AU, Jonas P, Sakmann B, Jack JJB (1994) Detailed passive cable models of whole-cell recorded CA3 pyramidal neurons in rat hippocampal slices. *J Neurosci* 14:4613-4638
- Manookin MB, Beaudoin DL, Ernst ZR, Flagel LJ, Demb JB (2008) Disinhibition combines with excitation to extend the operating range of the OFF visual pathway in daylight. *J Neurosci* 28:4136-4150
- Marc RE, Anderson JR, Jones BW, Sigulinsky CL, Lauritzen JS (2014) The AII amacrine cell connectome: a dense network hub. *Front Neural Circ* 8, 104. doi: 10.3389/fncir.2014.00104
- Masland RH (2012) The tasks of amacrine cells. *Visual Neurosci* 29:3-9
- Meyer A, Tetenborg S, Greb H, Segelken J, Dorgau B, Weiler R, Hormuzdi SG, Janssen-Bienhold U, Dedek K (2016) Connexin30.2: *in vitro* interaction with connexin36 in HeLa cells and expression in AII amacrine cells and intrinsically photosensitive ganglion cells in the mouse retina. *Front Mol Neurosci* 9:36. doi: 10.3389/fnmol.2016.00036
- Mills SL, Massey SC (1995) Differential properties of two gap junctional pathways made by AII amacrine cells. *Nature* 377:734-737
- Mørkve SH, Veruki ML, Hartveit E (2002) Functional characteristics of non-NMDA-type ionotropic glutamate receptor channels in AII amacrine cells in rat retina. *J Physiol* 542:147-165
- Münch TA, da Silveira RA, Siegert S, Viney TJ, Awatramani GB, Roska B (2009) Approach sensitivity in the retina processed by a multifunctional neural circuit. *Nat Neurosci* 12:1308-1316
- Murphy GJ, Rieke F (2008) Signals and noise in an inhibitory interneuron diverge to control activity in nearby retinal ganglion cells. *Nat Neurosci* 11:318-326
- Nörenberg A, Hu H, Vida I, Bartos M, Jonas P (2010) Distinct nonuniform cable properties optimize rapid and efficient activation of fast-spiking GABAergic interneurons. *Proc Natl Acad Sci USA* 107:894-899
- Oltedal L, Veruki ML, Hartveit E (2009) Passive membrane properties and

- electrotonic signal processing in retinal rod bipolar cells. *J Physiol* 587:829-849
- Perreault M-C, Raastad M (2006) Contribution of morphology and membrane resistance to integration of fast synaptic signals in two thalamic cell types. *J Physiol* 577:205-220
- Peters F, Gennerich A, Czesnik D, Schild D (2000) Low frequency voltage clamp: recording of voltage transients at constant average command voltage. *J Neurosci Meth* 99:129-135
- Pologruto TA, Sabatini BL, Svoboda K (2003) ScanImage: flexible software for operating laser scanning microscopes. *Biomed Eng Online* 2, 13
- Schaefer AT, Helmstaedter M, Sakmann B, Korngreen A (2003) Correction of conductance measurements in non-space-clamped structures: 1. Voltage-gated K<sup>+</sup> channels. *Biophys J* 84:3508-3528
- Schmidt-Hieber C, Jonas P, Bischofberger J (2007) Subthreshold dendritic signal processing and coincidence detection in dentate gyrus granule cells. *J Neurosci* 27:8430-8441
- Schubert T, Euler T (2010) Retinal processing: global players like it local. *Curr Biol* 20:R486-488
- Spruston N, Jaffe DB, Johnston D (1994) Dendritic attenuation of synaptic potentials and currents: the role of passive membrane properties. *Trends Neurosci* 17:161-166
- Spruston N, Stuart G, Häusser M (2016) Principles of dendritic integration. In: Stuart G, Spruston N, Häusser M (eds) *Dendrites*, 3rd edn. Oxford University Press, Oxford, pp. 351-398
- Stincic T, Smith RG, Taylor WR (2016) Time course of EPSCs in ON-type starburst amacrine cells is independent of dendritic location. *J Physiol* 594:5685-5694
- Strettoi E, Masland RH (1996) The number of unidentified amacrine cells in the mammalian retina. *Proc Natl Acad Sci USA* 93:14906-14911

- Strettoi E, Raviola E, Dacheux RF (1992) Synaptic connections of the narrow-field, bistratified rod amacrine cell (AII) in the rabbit retina. *J Comp Neurol* 325:152-168
- Strettoi E, Dacheux RF, Raviola E (1994) Cone bipolar cells as interneurons in the rod pathway of the rabbit retina. *J Comp Neurol* 347:139-149
- Szoboszlay M, Lőrincz A, Lanore F, Vervaeke K, Silver RA, Nusser Z (2016) Functional properties of dendritic gap junctions in cerebellar Golgi cells. *Neuron* 90:1043-1056
- Thompson SM, Masukawa LM, Prince DA (1985) Temperature dependence of intrinsic membrane properties and synaptic potentials in hippocampal CA1 neurons *in vitro*. *J Neurosci* 5:817-824
- Tian M, Jarsky T, Murphy GJ, Rieke F, Singer JH (2010) Voltage-gated Na channels in AII amacrine cells accelerate scotopic light responses mediated by the rod bipolar cell pathway. *J Neurosci* 30:4650-4659
- Trevelyan AJ, Jack J (2002) Detailed passive cable models of layer 2/3 pyramidal cells in rat visual cortex at different temperatures. *J Physiol* 539:623-636
- Trexler EB, Li W, Mills SL, Massey SC (2001) Coupling from AII amacrine cells to ON cone bipolar cells is bidirectional. *J Comp Neurol* 437:408-422
- Vaney DI (1991) Many diverse types of retinal neurons show tracer coupling when injected with biocytin or Neurobiotin. *Neurosci Lett* 125:187-190
- Vardi N, Smith RG (1996) The AII amacrine network: coupling can increase correlated activity. *Vision Res* 36:3743-3757
- Veruki ML, Hartveit E (2002a) AII (rod) amacrine cells form a network of electrically coupled interneurons in the mammalian retina. *Neuron* 33:935-946
- Veruki ML, Hartveit E (2002b) Electrical synapses mediate signal transmission in the rod pathway of the mammalian retina. *J Neurosci* 22:10558-10566
- Veruki ML, Hartveit E (2009) Meclofenamic acid blocks electrical synapses of retinal AII amacrine and ON-cone bipolar cells. *J Neurophysiol* 101:2339-2347

- Veruki ML, Mørkve SH, Hartveit E (2003) Functional properties of spontaneous EPSCs and non-NMDA receptors in rod amacrine (AII) cells in the rat retina. *J Physiol* 549:759-774
- Veruki ML, Oltedal L, Hartveit E (2010) Electrical coupling and passive membrane properties of AII amacrine cells. *J Neurophysiol* 103:1456-1466
- Vervaeke K, Lörincz A, Nusser Z, Silver RA (2012) Gap junctions compensate for sublinear dendritic integration in an inhibitory network. *Science* 335:1624-1628
- Vlasits AL, Morrie RD, Tran-Van-Minh A, Bleckert A, Gainer CF, DiGregorio DA, Feller MB (2016) A role for synaptic input distribution in a dendritic computation of motion direction in the retina. *Neuron* 89:1317-1330
- Wu C, Ivanova E, Cui J, Lu Q, Pan Z-H (2011) Action potential generation at an axon initial segment-like process in the axonless retinal AII amacrine cell. *J Neurosci* 31:14654-14659
- Yasuda R, Nimchinsky EA, Scheuss V, Pologruto TA, Oertner TG, Sabatini BL, Svoboda K (2004) Imaging calcium concentration dynamics in small neuronal compartments. *Sci STKE* p15
- Zandt B-J, Liu JH, Veruki ML, Hartveit E (2017) AII amacrine cells: quantitative reconstruction and morphometric analysis of electrophysiologically identified cells in live rat retinal slices imaged with multi-photon excitation microscopy. *Brain Struct Funct* 222:151-182

**Acknowledgements** Financial support from The Research Council of Norway (NFR 182743, 189662, 214216 to E.H.; NFR 213776, 261914 to M.L.V.) is gratefully acknowledged.

**Author contributions** B.J.Z. performed morphological reconstructions and compartmental modeling. M.L.V. and E.H. conceived and designed the experiments and performed electrophysiological recording and MPE microscopic imaging. B.J.Z., M.L.V. and E.H. interpreted data, made the figures, wrote the manuscript, and approved the final version of the manuscript. The experiments were done in the Department of Biomedicine, University of Bergen.

**Compliance with ethical standards** The use of animals in this study was carried out under the approval of and in accordance with the regulations of the Animal Laboratory Facility at the Faculty of Medicine at the University of Bergen (accredited by AAALAC International).

**Conflict of interest** The authors declare that they have no conflict of interest.

## Figure legends

**Fig. 1** Visual targeting, electrophysiological recording, multi-photon excitation (MPE) microscopy, and morphological reconstruction of AII amacrine cells in rat retinal slices.

**a** Infrared (IR) Dodt gradient contrast videomicrograph of an AII amacrine cell in a rat retinal slice. Arrowhead points to cell body of AII amacrine visible at the border between inner nuclear and inner plexiform layers. Apical dendrite of AII amacrine is visible as it descends into the inner plexiform layer. The retinal layers are indicated by abbreviations (OPL, outer plexiform layer; INL, inner nuclear layer; IPL, inner plexiform layer; GCL, ganglion cell layer). **b** Electrophysiological "signature" of AII amacrine cell during whole-cell voltage-clamp recording. Transient inward currents (*bottom* traces) correspond to unclamped action currents (escaping from voltage-clamp control) evoked by 5 mV depolarizing voltage pulses (5 ms duration; *top* traces) from a holding potential of -60 mV. **c** Maximum intensity projection (MIP) of complete image stack (after deconvolution) of AII amacrine cell (153 slices separated by 0.4  $\mu\text{m}$ ) acquired with MPE microscopy after filling the cell with the fluorescent dye Alexa 594 via the patch pipette (dye-filled pipette attached to cell body; *left*). MIP overlaid on image of retinal slice acquired with IR-laser scanning gradient contrast microscopy to show the position of the cell in the slice. **d** Shape plots of all electrophysiologically recorded and morphologically reconstructed AII amacrine cells ( $n = 13$ ). Five cells (top row, first cell in second row) are new to this study, while the others were included in a previous study from our laboratory (Zandt et al. 2017). All cells were filled with fluorescent dye during whole-cell recording in retinal slices, imaged with MPE microscopy and morphologically reconstructed. Cells have been rotated in XY plane as required to orient the long axis vertically. *Scale bars* 5  $\mu\text{m}$  (**a, c**), 10  $\mu\text{m}$  (**d**).

**Fig. 2** Complete and reversible block of electrical coupling between AII amacrine cells by 100  $\mu\text{M}$  meclofenamic acid (MFA). **a left**, IR differential interference contrast videomicrograph of a retinal slice with cell bodies of two neighboring AII amacrine cells and their recording pipettes (tips marked by vertical *white* arrows). **a right**, Same

slice visualized with fluorescence microscopy after filling cells with the fluorescent dye Alexa 594 via patch pipettes. MIP (along Z-axis) generated from wide-field fluorescence image stack after deconvolution. *Scale bar* 10  $\mu\text{m}$ . **b** Junctional conductance ( $G_j$ ) between two electrically coupled AII amacrine cells in **a** (dual, whole-cell voltage-clamp recording; same cell pair in **b-d**) during bath application and subsequent washout of 100  $\mu\text{M}$  MFA (applied in the extracellular solution during the period indicated by the shaded area,  $\sim 25$  min).  $G_j$  is calculated as the average of the conductance values measured for each direction of coupling (with voltage pulses applied to either cell 1 or 2). **c** Apparent membrane resistance ( $r_m$ ) for cells 1 and 2 as a function of time in the control condition, during application of MFA, and during and following washout of MFA. **d** Voltage-clamp holding current ( $I_{\text{hold}}$ ) as a function of time.

**Fig. 3** Linear membrane properties of AII amacrine cells. **a** Current responses (*bottom*; average of 100 trials) of an AII amacrine cell evoked by 20 ms voltage pulses (*top*) with different amplitudes, with current traces colored as a function of the applied voltage pulse amplitude: -10 mV (*red*), -5 mV (*light red*), +5 mV (*gray*), and +10 mV (*black*) relative to holding potential (-60 mV). **b** Current responses in **a** (same colors) were scaled with applied voltage pulse amplitude and superimposed to examine linearity. Superposition of current responses to -10 and -5 mV voltage pulses indicate that they scale linearly with voltage. Current responses to +5 and +10 mV revealed activation of voltage-gated currents and did not superimpose with the other current responses. Time scale expanded (relative to **a**) to display onset and initial decay of current transients with higher temporal resolution. *Inset* displays selected epochs (marked by broken line rectangle) at higher magnification. **c** Current responses evoked by the -10 and -5 mV voltage pulses were plotted against each other (after scaling with applied voltage pulse amplitude as in **b**) for corresponding points in time during a 19.9 ms time interval, starting 100  $\mu\text{s}$  after the onset of the voltage pulse stimulus. The straight line indicates a linear fit to the data points and has a slope of 0.98.

**Fig. 4** Estimating passive membrane properties after electrophysiological recording and morphological reconstruction of AII amacrine cells. **a** Current responses of AII amacrine cell (*bottom* traces; average of 50 trials) to -5 mV voltage pulse (20 ms; *top*) in the control condition with intact electrical coupling (*left*) and after blocking electrical coupling pharmacologically with MFA (*right*). Shape plot (*left*) generated from morphologically reconstructed AII amacrine. **b** Same as in **a**, but with time scale expanded to display decay of current response of AII amacrine cell (*black*) and of best-fitting, passive compartmental model (*red*) obtained either in the control condition (with intact electrical coupling; *left*) and after blocking electrical coupling with MFA (*right*). The compartmental model was obtained by directly fitting the current responses of the model evoked by voltage pulses to the experimental data in NEURON with four free parameters: specific membrane resistance ( $R_m$ ), membrane capacitance ( $C_m$ ), cytoplasmic resistivity ( $R_i$ ), and series resistance ( $R_s$ ). **c** Curve fit residual (difference between experimental and model current response in **b**) in the control condition (*left*) or in the presence of MFA (*right*). Because the curve fit residuals were dominated by noise, the traces were low-pass filtered (at 1 kHz; 2nd order Butterworth filter) to emphasize the difference between the two conditions. Notice the systematic deviation from the zero line in the control condition. **d** Improvement of goodness-of-fit for the compartmental model over time (with time zero corresponding to the establishment of the whole-cell configuration) corresponding to gradually increasing block of electrical coupling by MFA. Goodness-of-fit quantified by RMS error (square root of the mean of the squared residuals). Period of application of MFA in the extracellular solution indicated by the shaded area (**d-h**). **e-h** Time series plots to display the parameters  $R_m$  (**e**),  $C_m$  (**f**),  $R_i$  (**g**) and  $R_s$  (**h**) of the best-fit compartmental models as a function of time after establishing the whole-cell recording configuration and during gradually increasing block of electrical coupling by MFA (as in **d**).

**Fig. 5** Influence of the thickness of reconstructed neuron processes on passive membrane and cytoplasm properties obtained by compartmental model fitting. **a** Theoretical relationships between the difference between the reconstructed and true diameter of a neuronal process and the consequent deviation from the true value of the parameters  $R_i$ ,  $R_m$ ,  $\tau_m$  (membrane time constant), and  $C_m$ . **b-e** Relationships between the modal process diameter and specific membrane and cytoplasm properties for compartmental models of AII amacrine cells ( $n = 13$  cells). **b** Strong correlation between the inverse of the modal process diameter and  $C_m$ . Here, and in **c-e**, data points have been fitted with a straight line. **c** Weak correlation between the modal process diameter and  $R_m$ . **d** No correlation between the modal process diameter and  $\tau_m$ . **e** Strong correlation between the squared modal process diameter and  $R_i$ .

**Fig. 6** Directly estimating the membrane time constant ( $\tau_m$ ) with current clamp recording. **a**, *left*, Shape plot of the morphologically reconstructed AII amacrine cell that generated the voltage responses here and in **b - e**. **a** *right*, Voltage responses (change in membrane potential;  $\Delta V_m$ ) evoked by injecting short (2 ms, 20 pA; *black*; each trace average of 100 trials) and long (500 ms, 2 pA; *red*; each trace average of 100 trials) current pulses in whole-cell current-clamp recordings. Voltage responses aligned along X-axis by the end of the current pulse (corresponding to time zero) and normalized by the peak amplitude of each response. **b** Same as in **a**, but expanded with higher magnification around time zero. Notice faster initial decay of voltage response evoked by short (*black*) current pulse, corresponding to rapid charge redistribution. **c** Same as in **a** and **b**, with the (normalized) change in membrane potential ( $\Delta V_m$ ) displayed on a logarithmic axis to facilitate comparison of decay time course. Notice the almost linear decay in the semi-logarithmic plot and the similar decay of membrane potential for short (*black*) and long (*red*) current pulses following the initial charge redistribution (for the short pulse stimulation). **d** Decay of membrane potential response ( $\Delta V_m$ ) after injecting short current pulses ( $\pm 20$  pA; *black*). The decay phases

have been fitted with single-exponential functions (*red*). Each trace is the average of 100 individual trials. **e** Decay of membrane potential response ( $\Delta V_m$ ) after injecting long current pulses ( $\pm 2$  pA; *black*). The decay phases have been fitted with single-exponential functions (*red*). Each trace is the average of 100 individual trials. **f** Estimates of  $\tau_m$  during whole-cell recording of an AII amacrine cell (time zero corresponds to breaking into the cell and establishing the whole-cell recording configuration), first indirectly from  $R_m$  and  $C_m$  ( $\tau_m = R_m \times C_m$ ) during voltage-clamp recording (VC; continuous line) and gradual block of electrical coupling by MFA, and, subsequently (after complete block of electrical coupling), by fitting the decay of voltage responses evoked by current pulses during current-clamp recording (CC; circles) with single-exponential functions (from 5 to 200 ms following offset of the current pulses). Period of application of MFA in the extracellular solution indicated by the shaded area. **g** Relationship between  $\tau_m$  obtained directly from current-clamp recording and indirectly from voltage-clamp recording ( $n = 5$  cells for which stable periods with current-clamp recording were obtained). The rectangular box around each data point corresponds to  $\pm 2 \times$  SEM. The identity line (broken line) corresponds to identical values of  $\tau_m$  obtained with the two methods.

**Fig. 7** Signal attenuation between soma and dendritic processes of AII amacrine cells. **a** Shape plots of AII amacrine cell, color coded to display signal attenuation during computer simulation of sinusoidal current injection (0 and 100 Hz) either at soma (1, 2), at tip of lobular dendrite (3, 4) or at tip of arboreal dendrite (5, 6), as indicated by pipette location. For each case, the voltage response ( $\Delta V_{\text{measure}}$ ) at a given location was normalized by the response occurring at the site of injection ( $\Delta V_{\text{inject}}$ ;  $\Delta V_{\text{measure}} / \Delta V_{\text{inject}}$ ). Here and later,  $\Delta V_{\text{measure}} / \Delta V_{\text{inject}} = 1$  (*red* in the color code) corresponds to no attenuation and  $\Delta V_{\text{measure}} / \Delta V_{\text{inject}} = 0$  (*black* in the color code) corresponds to complete attenuation. **b** Voltage attenuation at the arboreal (continuous line) and the lobular (broken line) dendritic tip (as indicated in **a** by pipette location) as a function of the

frequency of a sinusoidal current stimulus injected at the soma. **c** Voltage attenuation at an arboreal dendritic tip as a function of the frequency of a sinusoidal current stimulus injected at the soma for all 13 morphologically reconstructed AII amacrine cells (Fig. 1d). **d** Voltage attenuation at a lobular dendritic tip as a function of the frequency of a sinusoidal current stimulus injected at the soma for all cells. **e** Voltage attenuation at soma as a function of the frequency of a sinusoidal current stimulus injected at the arboreal (continuous line) or the lobular (broken line) dendritic tip (as indicated in **a** by pipette location). **f** Voltage attenuation at soma as a function of the frequency of a sinusoidal current stimulus injected at an arboreal dendritic tip for all cells. **g** Voltage attenuation at soma as a function of the frequency of a sinusoidal current stimulus injected at a lobular dendritic tip for all cells. **h** Input impedance ( $Z_{in}$ ) at the three stimulus locations displayed for AII amacrine in **a** (soma, lobular dendrite, arboreal dendrite) as a function of the frequency of a sinusoidal current stimulus. **i** Input impedance at the soma as a function of the frequency of a sinusoidal current stimulus for all cells.

**Fig. 8** Signal transmission and spatial location in the dendritic tree of AII amacrine cells. **a** Space plots of local input impedance ( $Z_{in}$ ) for DC (0 Hz; *left*) and higher-frequency (100 Hz; *right*) signals as a function of spatial location in the dendritic tree of an AII amacrine cell (same cell as in Fig. 7).  $Z_{in}$  is plotted as a function of path distance from the soma and points on the same branch are connected by lines. **b** Space plots of signal transmission between a location in the dendritic tree and the soma for DC (0 Hz; *left*) and higher-frequency (100 Hz; *right*) signals, calculated as the ratio between the signal amplitude at the soma ( $V_{soma}$ ) and the signal amplitude at the stimulation site ( $V_{stim}$ ;  $V_{soma} / V_{stim}$ ). **c**, space plots of transfer impedance ( $Z_{tr}$ ) for DC (0 Hz; *left*) and higher-frequency (100 Hz; *right*) signals between the soma and the dendritic tree as a function of spatial location in the dendritic tree.

**Fig. 9** Voltage- and space-clamp control during electrophysiological whole-cell recording of an AII amacrine cell. **a** Shape plots of the membrane potential of a compartmental model of an AII amacrine cell during a computer-simulated, whole-cell, voltage-clamp recording at the soma with a homogeneously distributed and homogeneously activated, voltage-insensitive potassium conductance ( $g_K$ ) of increasing magnitude (added to the leak conductance of the passive, compartmental model). The voltage-clamp command potential ( $V_{com}$ ) was set to -40 mV, the series resistance ( $R_s$ ) was zero, and the potassium equilibrium potential ( $E_K$ ) was set to -80 mV.  $I_{clamp}$  indicates the measured voltage-clamp current for the combination of  $g_K$  and  $V_{com}$ .  $\Delta V_{RMS}$  indicates the root-mean-square of the deviation of the cell's membrane voltage from  $V_{com}$ . The local membrane potential is color coded, with *red* indicating no deviation from  $V_{com}$  and *black* indicating a deviation  $\geq 10$  mV of the membrane potential from  $V_{com}$  (more negative than -50 mV). The arrows labeled A and L in the leftmost shape plot indicate the location where synaptic conductance waveforms were injected for the simulations in **e-h**, corresponding to a lobular and an arboreal dendrite, respectively. **b** As in **a**, with  $I_{clamp}$  as a function of  $g_K$  for four different values of  $V_{com}$ . **c** As in **a**, with  $\Delta V_{RMS}$  as a function of  $g_K$  for four different values of  $V_{com}$  (here and in **d**, same order of  $V_{com}$  values from top to bottom as in **b**). **d** As in **a**, with  $\Delta V_{RMS}$  as a function of voltage-clamp current (induced by varying  $g_K$ ) for four different values of  $V_{com}$ . **e** Current responses obtained with simulation of whole-cell, voltage-clamp recording at the soma of AII amacrine (same cell as in **a**) and injection of a synaptic conductance waveform at the tip of an arboreal dendrite (arrow labeled A in **a**). The synaptic conductance waveform had a peak conductance of 480 pS, a 10 - 90% rise time of  $\sim 340 \mu s$  and a single exponential decay of  $\sim 760 \mu s$  (see Materials and methods) and was generated from a physiologically recorded glutamatergic, spontaneous EPSC (cf. Veruki et al. 2003). With perfect voltage clamp and a driving force of 60 mV, the synaptic conductance would result in a clamp current corresponding to the *red* trace. The simulations were repeated for a series of  $R_s$  values, ranging from  $\sim 0$  to 50 M $\Omega$  (with increments of 5 M $\Omega$ ), as well as a final trial with 100 M $\Omega$ . Notice the marked

distortion, increasing with increasing  $R_s$ , of the voltage-clamp currents recorded at the soma relative to the current obtained with perfect voltage clamp. **f** The waveforms in **e** have been normalized to their peak amplitudes for improved visualization of increasing temporal distortion. **g** As in **e**, but for injection of the synaptic conductance waveform at a proximal lobular dendrite (arrow labeled L in **a**). Notice markedly lower amplitude reduction and temporal distortion of voltage-clamp currents (relative to response obtained with perfect voltage-clamp control; *red* trace) compared to synaptic input at distal arboreal dendrite (in **e**). **h** As in **f**, but for current waveforms in **g** evoked by synaptic input at lobular dendrite.

**Table 1. Best-fit parameters obtained for AII amacrine cells (population data)**

	Mean	S.D.	Min.	Max.	Average total error (%)
Total area ( $\mu\text{m}^2$ )	1967	386	1300	2527	18.7
$C_m$ ( $\mu\text{F} \cdot \text{cm}^{-2}$ )	0.91	0.14	0.71	1.31	19.5
$R_m$ ( $\text{k}\Omega \cdot \text{cm}^2$ )	30.2	8.7	20.1	45.2	18.5
$R_i$ ( $\Omega \cdot \text{cm}$ )	198	62	82	279	34.2
$R_s$ ( $\text{M}\Omega$ )	25.0	11.3	15.5	50.8	10.5
$\tau_m$ (ms)	27.2	7.6	17.6	37.6	3.1
$R_{in}$ ( $\text{M}\Omega$ )	1647	524	853	2558	2.8
$C_{total}$ (pF)	17.8	3.7	10.8	22.2	0.7
$V_{rest}$ (mV)	-50.4	7.1	-59.1	-36.8	1.6
$V_{att}$ (0 Hz)	2.4%	1.1%	1.3%	5.1%	4.5
$V_{att}$ (100 Hz)	9.9%	4.7%	2.7%	20.5%	5.6
$V_{att}$ (1000 Hz)	61.9%	8.0%	41.4%	72.0%	2.2
Fit error (pA)	0.21	0.15	0.05	0.53	-

The electrophysiological data were obtained with whole-cell voltage-clamp recording after complete block of gap junction-mediated electrical coupling with MFA. Passive membrane parameters (specific membrane capacitance,  $C_m$ ; specific membrane resistance,  $R_m$ ; cytoplasmic resistivity,  $R_i$ ) and series resistance ( $R_s$ ) were obtained using NEURON's multiple run fitter to directly fit the response of each cell's morphological model to the physiological data obtained for the same cell. Other functional properties (membrane time constant,  $\tau_m$ ; input resistance,  $R_{in}$ ; total capacitance,  $C_{total}$ ; resting membrane potential,  $V_{rest}$ ) were calculated from the fitted parameters and the reconstructed morphology. The relative signal attenuation over the cell ( $V_{att}$ ) for inputs at the cell body (at 0, 100, and 1000 Hz) was calculated with NEURON's impedance function (see Results). The fit error is the RMS error, estimated as the square root of the

mean of the squared fit residuals (low-pass filtered at 1 kHz; see Fig. 4c). The total error was calculated as the sum of the estimates for random error (determined by bootstrapping) and systematic error (see Results).

**Table 2. Best-fit parameters obtained for AII amacrine cells (individual cells)**

Cell #	$C_m$ ( $\mu\text{F} \cdot \text{cm}^{-2}$ )	CV (%)	$R_m$ ( $\text{k}\Omega \cdot \text{cm}^2$ )	CV (%)	$R_i$ ( $\Omega \cdot \text{cm}$ )	CV (%)	$R_s$ ( $\text{M}\Omega$ )	CV (%)
1	0.71	18	26	15	149	17	16	-
2	0.86	15	43	15	223	31	16	18
3	0.90	20	36	19	263	31	51	5
4	0.88	18	29	17	210	24	21	11
5	0.88	21	20	19	212	34	37	7
6	0.83	22	45	21	94	39	24	9
7	1.31	22	23	20	159	36	25	10
8	1.08	23	22	23	82	56	16	22
9	0.84	18	23	18	279	33	43	7
10	0.83	19	24	17	189	28	16	-
11	0.93	19	40	19	264	36	19	19
12	0.87	20	25	19	223	40	23	16
13	0.90	19	36	18	224	39	20	13
Mean $\pm$ S.D.	$0.91 \pm 0.14$	20	$30 \pm 9$	19	$198 \pm 62$	34	$25 \pm 11$	12

The electrophysiological data were obtained with whole-cell voltage-clamp recording after complete block of gap junction-mediated electrical coupling with MFA. Passive membrane parameters ( $C_m$ ,  $R_m$ ,  $R_i$ ) and  $R_s$  were obtained using NEURON's multiple run fitter to directly fit the response of each cell's morphological model to the physiological data obtained for the same cell. For two cells (#1 and #10), the unconstrained estimate for  $R_s$  was  $< R_{\text{pip}} \times 2$  and  $R_s$  was therefore constrained to be  $\geq R_{\text{pip}} \times 2$  during fitting and is indicated without corresponding estimates of error. Statistical random errors in the best-fit parameters were estimated by bootstrap analysis of the physiological responses (see Methods). For a given original data set, 100 synthetic data sets were used for model fitting in NEURON to obtain the 100 best-fit

values for each parameter and the variability of the best-fit parameter values is given by the coefficient of variation (CV).

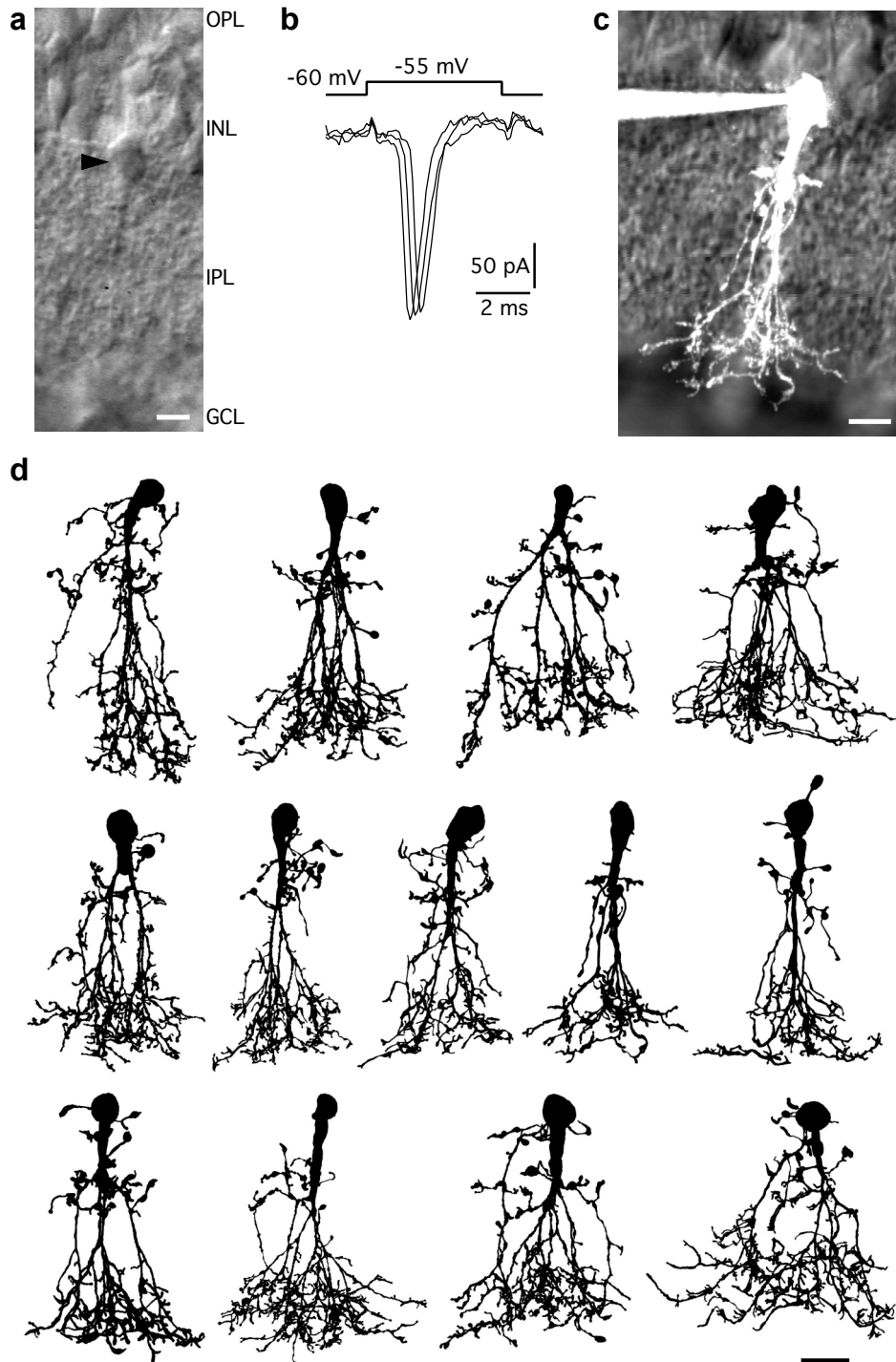


Figure 1 (Zandt et al.)

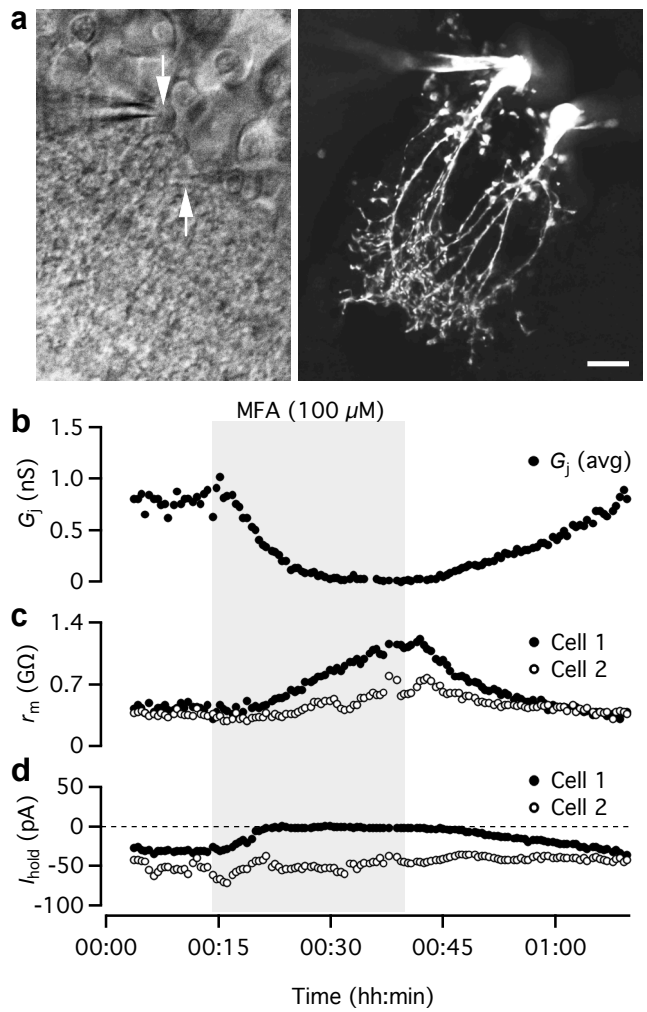


Figure 2 (Zandt et al.)

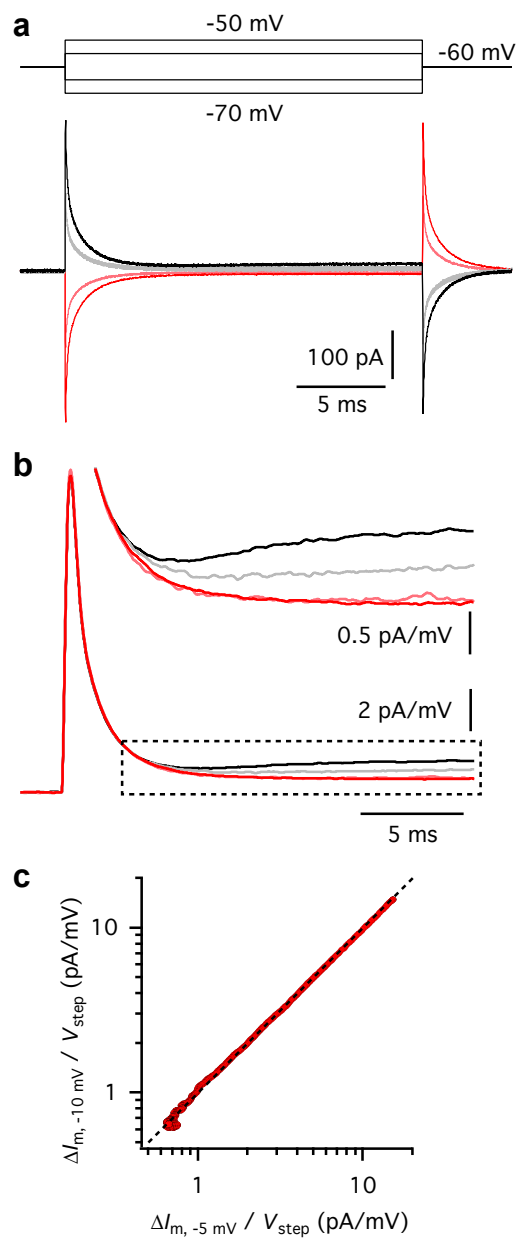


Figure 3 (Zandt et al.)

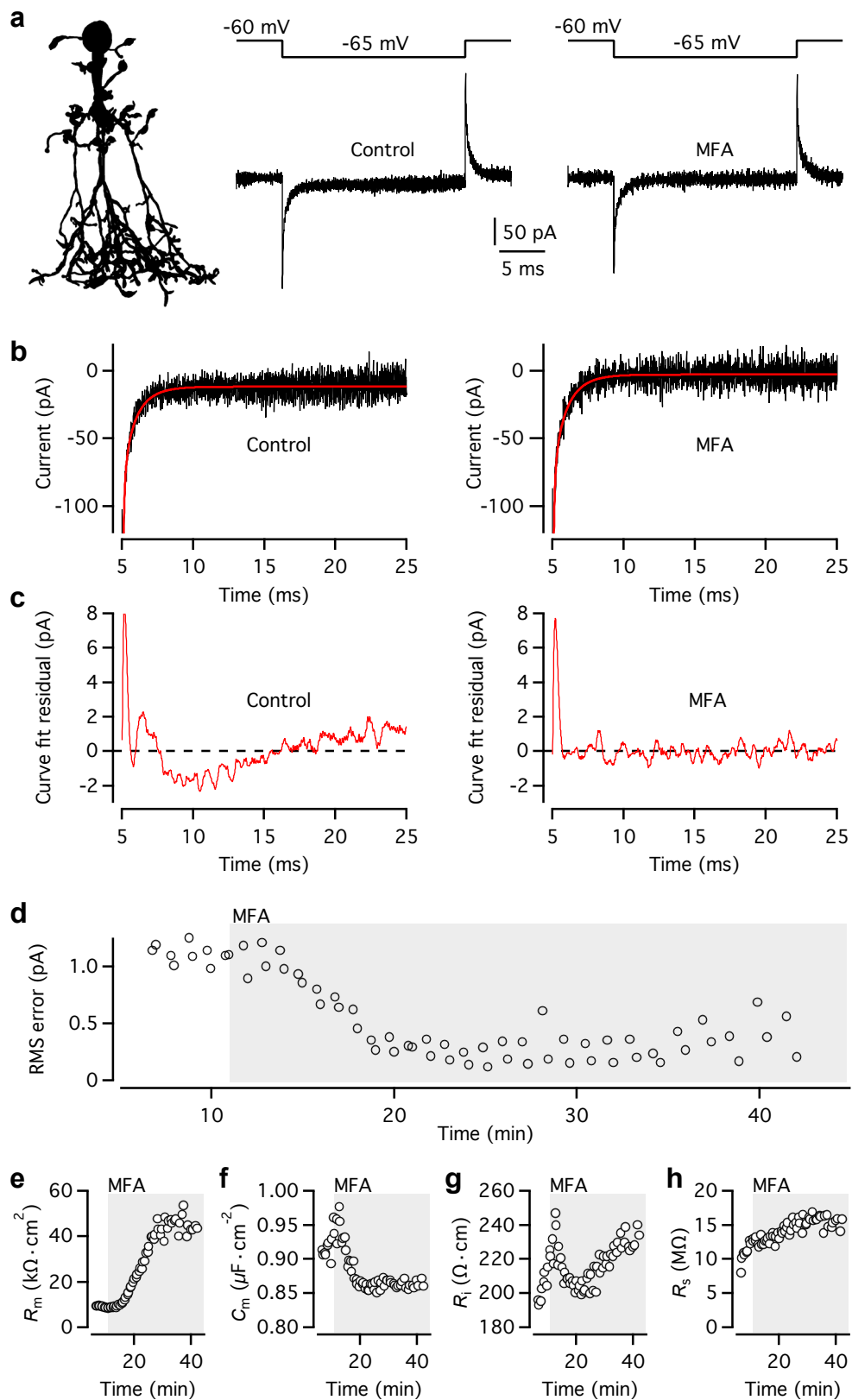


Figure 4 (Zandt et al.)

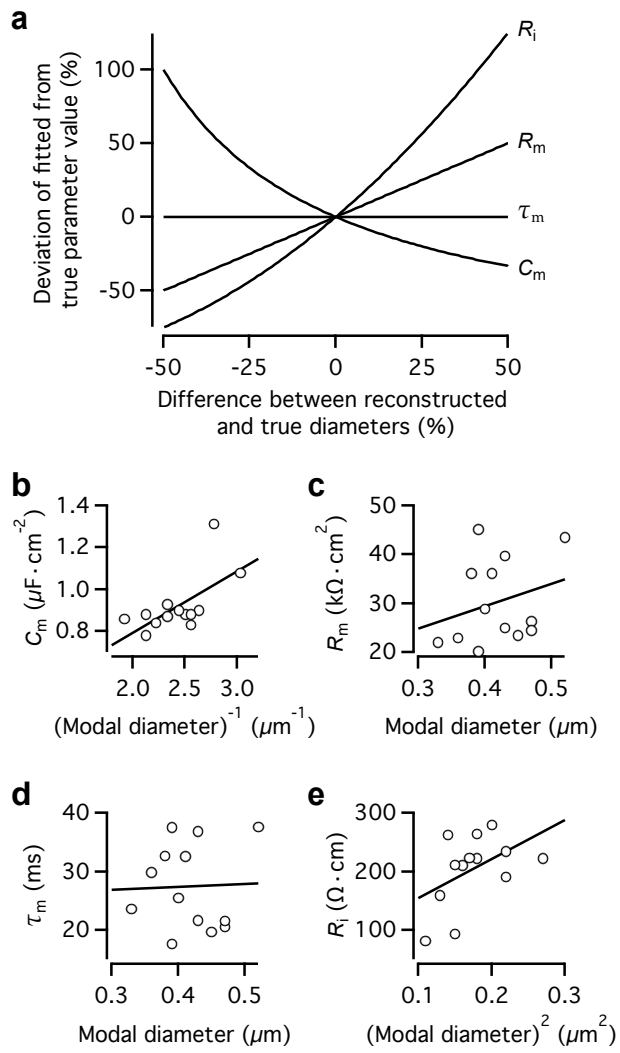


Figure 5 (Zandt et al.)

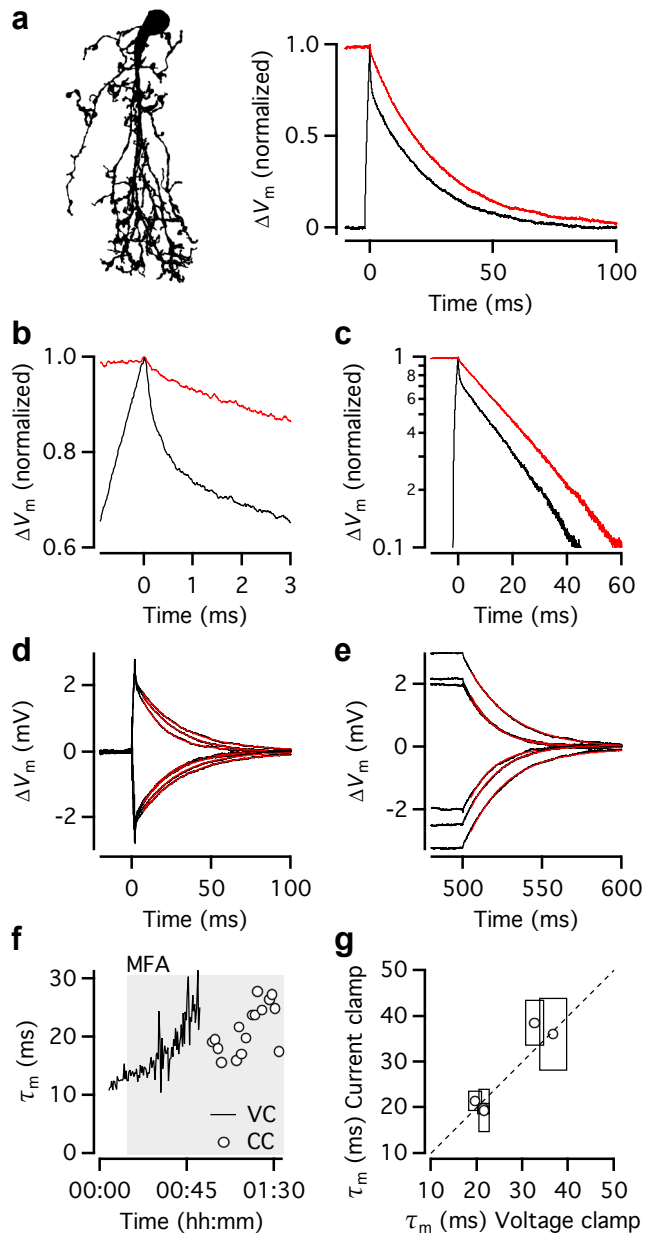


Figure 6 (Zandt et al.)

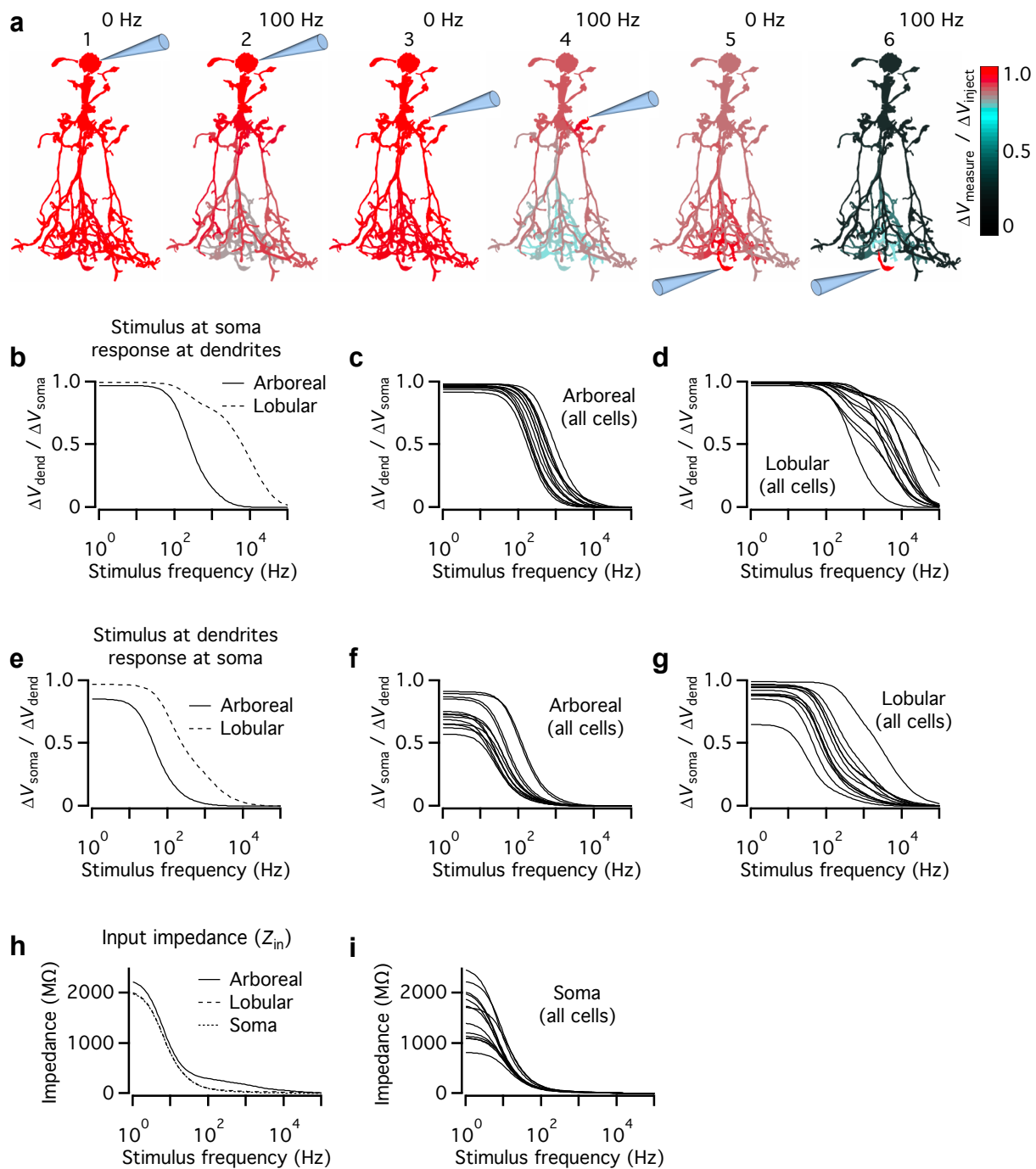


Figure 7 (Zandt et al.)

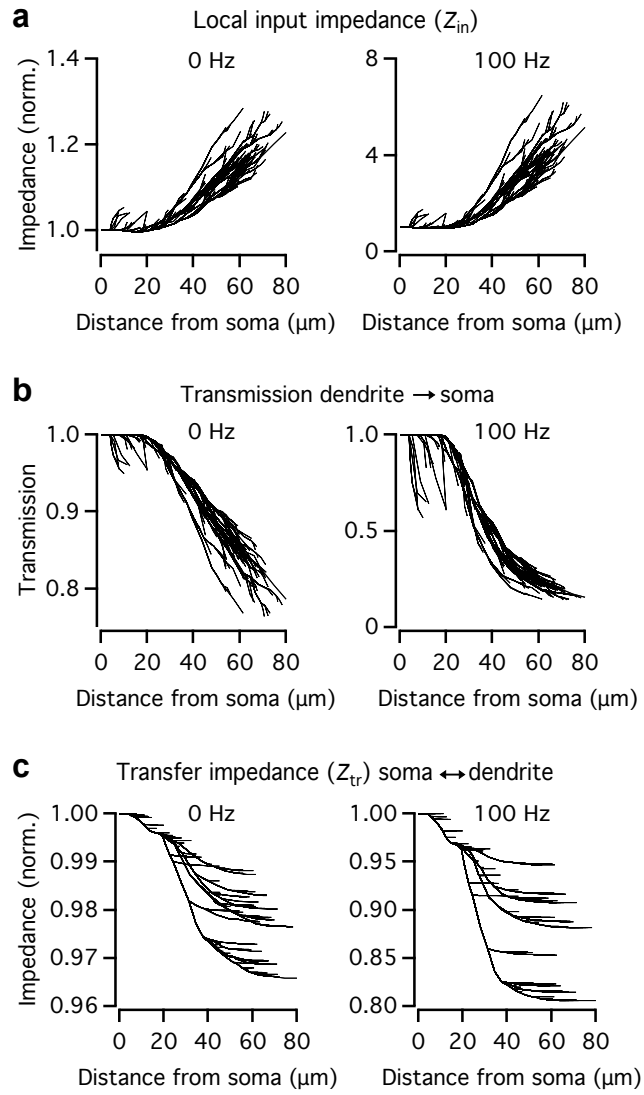


Figure 8 (Zandt et al.)

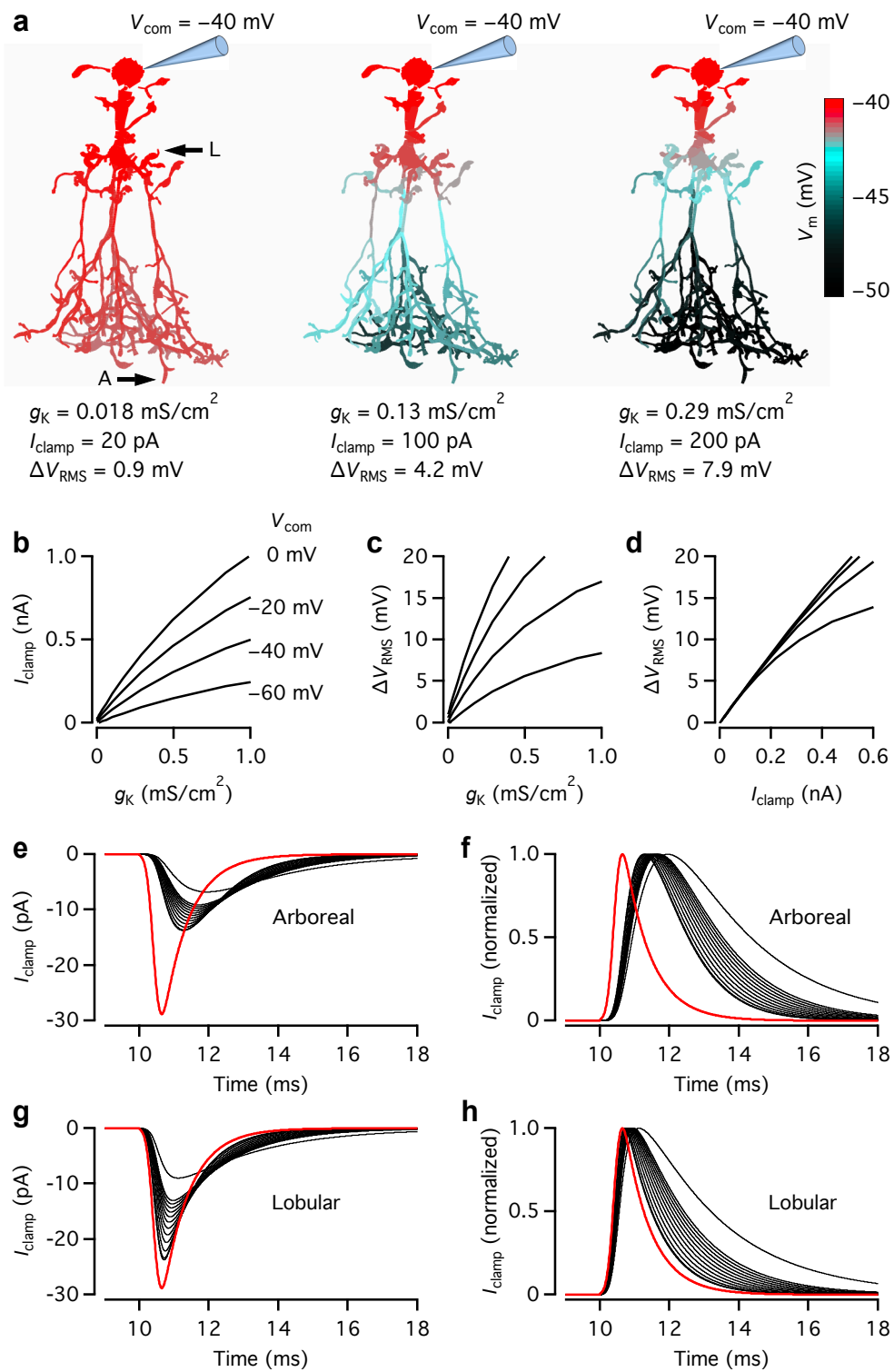


Figure 9 (Zandt et al.)